IEEE Access
Multidisciplinary | Rapid Review | Open Access Journal

Received May 29, 2020, accepted June 16, 2020, date of publication June 23, 2020, date of current version July 3, 2020.

Digital Object Identifier 10.1109/ACCESS.2020.3004439

Trajectory Planning for Navigation Aiding of Autonomous Underwater Vehicles

ØYSTEIN STURE[1], PETTER NORGREN[1], (Graduate Student Member, IEEE), AND MARTIN LUDVIGSEN[1,2,3]

[1]Department of Marine Technology, Faculty of Engineering, Norwegian University of Science and Technology (NTNU), 7052 Trondheim, Norway
[2]Centre for Autonomous Marine Operations and Systems, Department of Marine Technology, Norwegian University of Science and Technology (NTNU), 7491 Trondheim, Norway
[3]Arctic Technology Department, The University Centre in Svalbard (UNIS), 9171 Longyearbyen, Norway

Corresponding author: Øystein Sture (oystein.sture@ntnu.no)

This work was supported by the Research Council of Norway (Norges Forskningsråd, NFR) under Grant 247626 (MarMine) and Grant 276730 (The Nansen Legacy).

ABSTRACT Autonomous underwater vehicles can perform seabed surveys with a higher resolution and quality than from equivalent ship-mounted sensors. Although high-grade inertial navigation systems aided by Doppler velocity logs can operate without external position references for extended durations, this may still be required to meet survey specifications. This paper presents a trajectory planning algorithm for an autonomous surface vessel with the purpose of aiding the navigation of one or multiple underwater vehicles using ultra-short baseline acoustic positioning. The trajectory planning problem is formulated as a nonlinear program for the single-vehicle tracking scenario and mixed-integer nonlinear program for tracking of multiple vehicles. In the absence of external acoustic positioning, the horizontal uncertainties of all targets increase as functions of time and heading. The optimal placement of the surface vessel is calculated by considering the propagated acoustic measurement uncertainty, which varies according to the range and direction towards the target. The trajectories are generated by minimizing the uncertainty of all targets, while also considering penalties on the control inputs and obeying vessel kinematics. The approach is demonstrated through a series of simulations.

INDEX TERMS Acoustic measurements, autonomous vehicles, marine navigation, optimal control, path planning, position measurement, trajectory optimization, unmanned underwater vehicles.

I. INTRODUCTION

Autonomous underwater vehicles (AUVs) are untethered sensor carrying platforms capable of performing surveys in high proximity to the seabed. Moving the sensor carrying platform closer to the seabed can increase the resolution of the collected data significantly. This may be a requirement for certain applications, such as geomorphological studies where small-scale features of interest are not resolved in sufficient detail by hull-mounted instruments on ships. Examples of such applications may be the study of erosive processes over time, submarine landslides, hydrothermal vents, mid-ocean ridges, mud volcanoes and cold-water coral mounds [1].

Microwaves are absorbed rapidly in water, and a large caveat with data collection on underwater vehicles is the loss of global navigation satellite systems (GNSS) for positioning. AUVs equipped with state of the art inertial navigation systems (INS) may operate for extended durations with an external velocity reference from a Doppler velocity log (DVL). These measurements can be fused using a probabilistic state estimation filter, e.g. a Kalman filter. For high-end DVL-INS systems, the main contributors to horizontal position drift are errors in body-fixed velocities and heading due to low-frequency errors of the DVL and gyro bias dynamics. The best DVL-INS systems can achieve a drift of 0.1% of distance traveled when running in a straight line with bottom lock, which is the worst-case scenario in terms of bias estimation [2]. Micro delta-position aiding can provide a pseudo-velocity measurement with less long-term drift than the DVL, where a displacement as measured by a synthetic aperture sonar or camera is used [3]. Instruments capable of bathymetric measurements may also be used along with a known map in terrain aided navigation (TAN) or previously visited locations through simultaneous localization

The associate editor coordinating the review of this manuscript and approving it for publication was Jason Gu.

and mapping (SLAM) techniques [4]. These approaches are promising but may have trouble with robustness due to sensor outliers and ambiguities.

For surveys performed at modest depths, an alternative strategy is to periodically resurface for a position update. This may not be feasible given mission constraints, ship traffic, survey depth, and is perhaps undesirable due to the interruption of data collection. For deep-sea surveys where the AUV operates for long durations without a DVL bottom lock during the dive and ascent, or instances where the INS system is not providing acceptable performance, external acoustic position references can be used. The time of flight of an acoustic wave relative to a transducer with a known position is then used together with a measured sound of speed in water to estimate the position. Multiple acoustic measurements are combined to compute this estimate; either by measuring distinct pulses or by measuring the same pulse multiple times in a baseline of transducers. The former is known as single transponder navigation or virtual baseline navigation, which requires relative movement between the target and transponder to resolve the direction [2]. When the baseline in the latter is made up by multiple integrated transducers, it is referred to as ultra-short baseline (USBL) systems. In this work we focus on the USBL acoustic measurement principle, where a measured range and direction is used to estimate the position. The transducer is assumed to be mounted on a movable surface vessel, capable of following the underwater vehicle throughout its mission. Pairing an autonomous underwater vehicle with an autonomous surface vessel (ASV) acting as a communication and navigation aid (CNA) has been regarded as a natural step forward in automating surveys and freeing the AUV from the survey vessel. Recently, a concept where an underwater vehicle is launched and recovered from an autonomous surface vehicle has been demonstrated, further removing the need for a manned ship during launch, recovery, and transit [5]. Long-term deployments of a CNA across multiple AUV dives have been demonstrated by equipping a Wave Glider ASV, utilizing wave energy for propulsion, with acoustic modems and satellite communications [6]. CNAs have been used to provide persistent communications across a wide range of unmanned underwater, surface, and aerial vehicles [7], [8].

In this work, the propagated measurement uncertainty is derived based on uncertainties in the orientation of the surface vessel, measured acoustic direction, and measured acoustic range. This is in turn used to solve the path planning problem for an ASV in order to provide positioning updates to one or more underwater vehicles. The uncertainty of each vehicle is tracked in order to generate paths that weight the minimization of uncertainty against the energy expenditure of the vessel, while obeying kinematic constraints. The path planning problem is formulated as a nonlinear program (NLP) in the CasADi symbolic math and algorithmic differentiation framework [9]. Two formulations are proposed. The first assumes that all targets are continuously ranged using interleaved measurements, while the second makes an explicit decision of which target to track. The latter results in a mixed-integer nonlinear program (MINLP). The NLP is solved using the IPOPT CasADi backend [10], and the MINLP is solved using the BONMIN CasADi backend [11], [12]. The Harwell Subroutine Library (HSL) MA57 linear solver is used for both backends [13].

A. RELATED WORK

This work deals with the question of where to optimally position the topside vehicle in order to minimize the horizontal uncertainty of one or more underwater vehicles. Previous research has primarily focused on range-only acoustic localization. Since range-only measurements only places the target on a sphere surrounding the recipient, the relative direction between the target and surface vessel must change in order to bound the navigational drift. Although the measurement principle differs, there are similar considerations to be made for the path planning. An early development for a range-only solution was repeating patterns of zig-zag motion or circular motion around the horizontal location of the target underwater vehicle [14]. While a heuristic policy such as this may bound the navigational drift for a single vehicle, it does not minimize the fuel consumption or directly extend to a multi-vehicle tracking scenario. If the surface vessel is also used to collect complementary data (e.g. water-column acoustic profiling), the data quality may also be impacted. To account for these aspects in a planning algorithm, it is necessary to quantify the current uncertainty of the target vehicles, as well as a method to evaluate the reduction in uncertainty for a given trajectory. Waypoint generation based on the difference between the prior and posterior covariance matrices has been demonstrated [15]. There, the reduction in uncertainty was evaluated over a grid of reachable waypoints. The grid extent was determined by the maximum speed of the vehicle. At each step the waypoint yielding the largest reduction in variance was selected greedily. This enabled the algorithm to consider tracking of multiple vehicles, but suboptimal choices could be made depending on the paths of the target vehicles due to the one-step greedy planning. Later, a multi-step path planner was demonstrated over a set of discrete turn angles [16]. Two proposed algorithms were presented, one where the path planning problem was solved through Dynamical Programming (DP) over a finite horizon, and another where a Markov Decision Process (MDP) was used to pre-compute a heuristic decision policy. The sum of the variance along the major and minor axes of the posterior covariance matrix at each step was used as a cost function when learning the MDP policy. The two underwater vehicles were assumed to operate at the same fixed depth. More recently, a path planning approach based on a priority based random expansion of possible paths was developed [17]. The presented algorithm samples new points within a feasible circle, limited by the upper speed of the vehicle. Expansion continues along a predetermined number of best samples, selected in a greedy manner based on a cost function. The cost function used was composed of two terms. The first penalized the angle between the major axis of the covariance ellipse

and the direction towards the vehicle in the horizontal plane. The second added a penalty when the distance to the vehicle was above or below a fixed threshold. The time-evolution of the covariance matrix over the planning horizon was simulated by an extended Kalman filter (EKF) without considering the depth of the vehicle. The cost function was evaluated for a discrete set of times for every ping, thus indirectly optimizing over a set of discrete speeds.

Aside from considering USBL instead of range-only measurements, we improve on the previous work in one or more of the following areas. First, the vertical position of the underwater vehicle is considered in the propagation of uncertainty. The vehicle depth can also vary throughout the planning horizon. The path planning problem is discretized in time, but the decision variables are continuous. We include an energy penalty term as a function of vessel speed, enabling a trade-off between reduction in uncertainty and energy expenditure. The effect of an offset in the sound velocity profile on the measurements is also considered.

B. INS-USBL LOCALIZATION: ERROR SOURCES

In this section we highlight some of the primary sources of localization errors in a USBL-INS setting. We are primarily concerned with errors that can be influenced through the position of the surface vessel. More complete treatments of the uncertainties for hydrographic surveys are available [18], [19]. We assume that the involved systems are calibrated, and that no large discrepancies exist in the mounting offsets and orientations of the sensors.

The underwater vehicle follows its planned path based on an estimate of its position, with an associated uncertainty. The USBL system measures the propagation time, elevation and bearing to the underwater vehicle. Since the USBL modem is rigidly attached to a surface vessel, the roll, pitch, heading, and position of the surface vehicle must also be estimated to compute the position of the underwater vehicle. All these measurements have some degree of uncertainty. The speed of sound in water is used with the time measurements to compute the distance to the target. Generally, the speed of sound varies with depth due to a changing water density and compressibility. This is described through a sound velocity profile (SVP), typically calculated based on conductivity-temperature-depth (CTD) measurements or measured directly using a sound speed probe. The SVP can also be used to correct for acoustic ray-bending, which occurs if the SVP has a non-zero vertical gradient. For measurements near the vertical (nadir), this effect is negligible, but becomes progressively worse for larger elevation angles. Even if the SVP is measured accurately initially, the true profile may change over time or upon moving to a new location. Outliers may occur due to multi-path propagation, in which the acoustic wavefront is received via the seabed, surface, or floating objects such as icebergs. Multi-path propagation is not addressed in this work, and these events are assumed to be discarded by the underlying system.

The presence of systematic errors in the INS and USBL system can be divided into the following four scenarios under steady-state conditions. These are illustrated in Fig. 1.

1) UNBIASED INS AND UNBIASED USBL

The USBL system applies accurate sound-speed and ray-bending corrections. Given regular acoustic position updates, the AUV correctly estimates the biases in its body-fixed velocity and heading. The USBL measurements and INS estimates are in agreement.

2) BIASED INS AND UNBIASED USBL

The navigational sensors are either of poor quality or the INS is incorrectly tuned, and the AUV INS is therefore unable to estimate its bias states. The AUV continuously drifts away from its estimated position. At every USBL update, the estimated position jumps towards the USBL update. The navigational drift is still bounded, but has a periodic component determined by the magnitude of the bias states and the rate and quality of the acoustic measurements.

3) UNBIASED INS AND BIASED USBL

The USBL system applies the wrong overall sound speed or applies the wrong ray-bending corrections. Given acoustic position updates that are biased, but consistent, the INS tends towards the biased position. For example, if the topside vessel and underwater vehicle are moving in a fixed formation in the same direction.

4) BIASED INS AND BIASED USBL

As the previous scenario, the USBL system includes inherent biases depending on the acoustic conditions, and the AUV INS does also *not* fully take all sources of bias into account. Normally we operate in this scenario to a varying degree.

C. PRELIMINARIES

Matrices are written in bold capital letters and vectors are written in bold small letters. The short-hand notation c_ψ and s_ψ is used for cosines and sines with respect to the specified angle, ψ. A variable in the Euclidean space with dimension n is denoted $\mathbb{R}^n$, while matrices of dimension $n \times m$ are denoted $\mathbb{R}^{n\times m}$. The time derivative of a variable $x(t)$ is denoted $\dot{x}$. Superscript in curly brackets denotes the reference frame to which a given vector is expressed. For example, $p^{\{n\}}$ is a position in the north-east-down (NED) frame. The reference frames used are: NED (n), BODY (b), and USBL (u). A rotation matrix $\boldsymbol{R}_a^b \in \mathrm{SO}(3)$ between reference frames uses a subscript for the frame transformed from, and superscript for the frame transformed to. For example, rotating from BODY to NED is denoted $\boldsymbol{R}_b^n(\boldsymbol{\Theta}) = \boldsymbol{R}_{z,\psi}\boldsymbol{R}_{y,\theta}\boldsymbol{R}_{x,\phi}$ where $\boldsymbol{\Theta} = [\phi, \theta, \psi]^T$ is the Euler angle parametrization following the zyx-convention. The same notation is used for rotation by

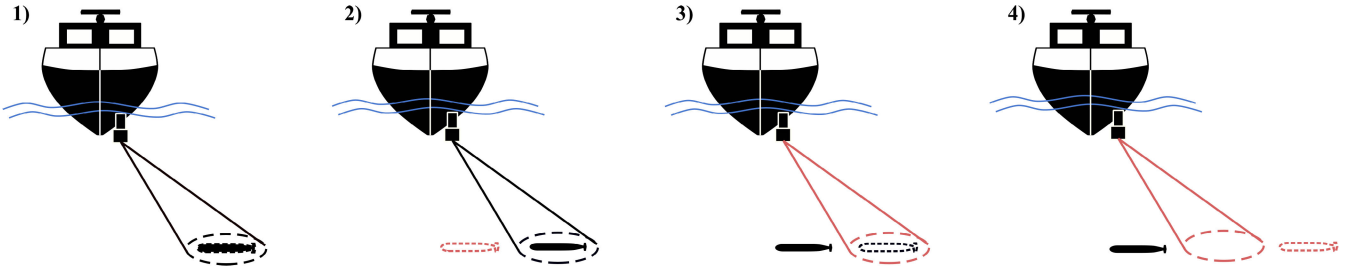

FIGURE 1. Four different scenarios involving systematic biases in the top-side acoustic positioning system and on-board inertial navigation system. The true vehicle position is shown in black, the estimated position of the INS system is shown with a dashed outline, and the USBL position estimate is shown as an elliptical projection onto the apparent position of the vehicle. Red is used to indicate an inherent bias. The illustrations are 1) Unbiased USBL and INS, 2) Unbiased USBL and biased INS, 3) Biased USBL and unbiased INS, 4) Biased USBL and INS.

other angles about the same principal axes.

$$\underbrace{\begin{bmatrix} 1 & 0 & 0 \\ 0 & c_\phi & -s_\phi \\ 0 & s_\phi & c_\phi \end{bmatrix}}_{\boldsymbol{R}_{x,\phi}} \underbrace{\begin{bmatrix} c_\theta & 0 & s_\theta \\ 0 & 1 & 0 \\ -s_\theta & 0 & c_\theta \end{bmatrix}}_{\boldsymbol{R}_{y,\theta}} \underbrace{\begin{bmatrix} c_\psi & -s_\psi & 0 \\ s_\psi & c_\psi & 0 \\ 0 & 0 & 1 \end{bmatrix}}_{\boldsymbol{R}_{z,\psi}}$$

We additionally take the matrix $\boldsymbol{R}_2 \in \mathrm{SO}(2)$ to mean the rotation matrix in the (horizontal) plane for a possibly time-varying heading.

$$\boldsymbol{G}(t) = \boldsymbol{R}_2(\psi(t)) = \begin{bmatrix} c_{\psi(t)} & -s_{\psi(t)} \\ s_{\psi(t)} & c_{\psi(t)} \end{bmatrix}$$

The skew-symmetric matrix $\boldsymbol{S}(\boldsymbol{\lambda}) \in \mathrm{SS}(3)$ denotes the vector cross product operator defined as follows.

$$\boldsymbol{S}(\boldsymbol{\lambda}) = \begin{bmatrix} 0 & -\lambda_3 & \lambda_2 \\ \lambda_3 & 0 & -\lambda_1 \\ -\lambda_2 & \lambda_1 & 0 \end{bmatrix}, \quad \boldsymbol{\lambda} = \begin{bmatrix} \lambda_1 \\ \lambda_2 \\ \lambda_3 \end{bmatrix}$$

The derivative of a rotation matrix $\boldsymbol{R}_p(f(\theta))$ with respect to an angle θ about a principal axis is equivalent to matrix multiplication by a skew-symmetric matrix, where $\vec{e}$ is the basis vector corresponding to the principal axis of rotation.

$$\frac{d}{d\theta}\boldsymbol{R}_p(f(\theta)) = \boldsymbol{S}\left(\frac{df}{d\theta}\vec{e}\right)\boldsymbol{R}(f(\theta))$$

II. METHODS

In this section, the approach taken to solve the path planning problem is described. Kinematic models are used both for the surface vessel and the underwater vehicle. The kinematic model for the surface vessel is used in the motion planning to compute the response in position and heading to inputs in forward velocity and heading rate of change. The underwater vehicle model on the other hand is not used directly during optimization but is used to propagate the position forwards in time along the planned mission path. The result of this simulation is input into the path planning problem and assumed to be fixed. Ambiguity in the planned path of the vehicle is not considered, and the planned waypoints of the vehicle is therefore assumed to be known. The plan can either be exchanged prior to launch or over an acoustic link, where the latter allows for online replanning in response to dynamic mission objectives. A simple error model in terms of uncertainty in the body-fixed linear velocities is described and used to represent the increase in horizontal uncertainty between USBL updates. An expression for the propagated uncertainty for the acoustic positioning is derived based on linearization of the measurement equation. Finally, the path planning problem for a surface vessel following one or more underwater vehicles is presented in the form of a non-linear program (NLP).

A. SURFACE VESSEL KINEMATIC MODEL

The planning horizon for the tracking objective formulated in this work is performed over relatively long time horizons. For this reason the short-term dynamics becomes less important. A simple underactuated kinematic model of the vessel is therefore adopted to represent physical constraints. The state of the vehicle is taken to be the north position, east position, and heading respectively; $\boldsymbol{\eta}_S = [N, E, \psi]^T$. The inputs to be calculated are the forward velocity (surge) and yaw rate; $\boldsymbol{\nu}_S = [u, r]^T$.

$$\dot{\boldsymbol{\eta}}_S = \boldsymbol{\mathcal{J}}(\boldsymbol{\eta}_S)\boldsymbol{\nu}_S = \begin{bmatrix} c_\psi & 0 \\ s_\psi & 0 \\ 0 & 1 \end{bmatrix} \begin{bmatrix} u \\ r \end{bmatrix} \tag{1}$$

The vessel is assumed to have negligible side-slip and lateral motion due to currents.

B. UNDERWATER VEHICLE KINEMATIC SIMULATION

The following model is used to simulate the underwater vehicle towards a known set of waypoints. It is propagated forwards in time according to a kinematic vehicle model with north position, east position, depth, pitch angle, heading angle as states; $\boldsymbol{\eta}_U = [N, E, D, \theta, \psi]^T$. The inputs are surge velocity, sway velocity, pitch rate, and yaw rate; $\boldsymbol{\nu}_U = [u, v, q, r]^T$.

$$\dot{\boldsymbol{\eta}}_U = \boldsymbol{\mathcal{J}}(\boldsymbol{\eta}_U)\boldsymbol{\nu}_U = \begin{bmatrix} c_\psi c_\theta & -s_\psi & 0 & 0 \\ s_\psi c_\theta & c_\psi & 0 & 0 \\ -s_\theta & 0 & 0 & 0 \\ 0 & 0 & 1 & 0 \\ 0 & 0 & 0 & c_\theta^{-1} \end{bmatrix} \begin{bmatrix} u \\ v \\ q \\ r \end{bmatrix} \tag{2}$$

In the model above, we assume the underwater vehicle to be passively stabilized in roll with negligible roll dynamics. Taking the kinematic equations in 6 degrees of freedom as a

starting point [20], the model can be derived by solving for $\dot{\phi} = 0$ and taking this to be the input to the body-fixed angular velocity about the forward axis, p. Setting the initial value of the vehicle roll and heave linear velocity to be zero, the model simplifies to the above. The inputs are computed based on path following using line-of-sight (LOS) control, decoupled in the horizontal and vertical plane [21]. The kinematic model ensures that the generated trajectories have continuous first derivatives. Bounds should be placed on the input variables to approximately reflect the physical parameters of the system.

C. UNDERWATER VEHICLE ERROR MODELING

The horizontal drift in position of an AUV aided by external velocity measurements from a Doppler velocity log (DVL) is mainly determined by low frequency errors of the DVL (alignment, sound speed scaling) and heading error (gyro bias dynamics, magnetic deviation) [2]. The survey pattern may also influence the long-term drift, as velocity errors become observable during turns due to the centripetal acceleration. Biases can also cancel out if the survey pattern is designed with alternating directions. Here we consider the worst-case scenario, straight-line navigation, and derive a simple error model given uncertainties in the body-fixed velocity and heading.

$$\begin{bmatrix} \dot{N} + \delta\dot{N} \\ \dot{E} + \delta\dot{E} \end{bmatrix} = \boldsymbol{R}_2(\psi + \delta\psi) \begin{bmatrix} u + \delta u \\ v + \delta v \end{bmatrix} \tag{3}$$

The angle sum trigonometric identities are used with a first-order small-angle approximation to the heading deviation $\delta\psi$.

$$c_{\psi+\delta\psi} \approx c_\psi - \delta\psi s_\psi, \quad s_{\psi+\delta\psi} \approx s_\psi + \delta\psi c_\psi$$

The nominal lateral velocity is taken to be zero ($v = 0$), since the focus is on under-actuated vehicles with primarily forward thrust and negligible side-slip. The deterministic part of the rotation matrix can then be separated out.

$$\begin{bmatrix} \dot{N} + \delta\dot{N} \\ \dot{E} + \delta\dot{E} \end{bmatrix} = \boldsymbol{R}_2(\psi) \left(\begin{bmatrix} u + \delta u \\ \delta v \end{bmatrix} + \delta\psi \begin{bmatrix} -\delta v \\ u + \delta u \end{bmatrix} \right) \tag{4}$$

The cross-terms $\delta\psi\delta u$ and $\delta\psi\delta v$ are considered to be negligible compared to the other terms since they are products of two small quantities. Keeping only the non-deterministic terms leads to the error model below.

$$\begin{bmatrix} \delta\dot{N} \\ \delta\dot{E} \end{bmatrix} = \boldsymbol{R}_2(\psi) \begin{bmatrix} \delta u \\ \delta v + \delta\psi u \end{bmatrix} \tag{5}$$

The long-term accuracy in the DVL velocity can be described by $\sigma_{\delta u} = \kappa u + \epsilon$ where κ describes errors that scale with the velocity and a constant additive noise term ϵ [22]. Note that these specifications include a wide range of effects, and interpreting them as normally distributed uncorrelated noise is not correct in a statistical sense. It does however help in defining an approximate expectation on the long-term deviation. Increasing the frequency of the DVL generally reduce these errors, but also the attainable range. Modern DVLs with 200 m range can for example have scale factors κ between 0.002 and 0.004, and $\sigma(\epsilon)$ between 1 mm/s to 2 mm/s [2].

The nature of the heading error depends on the measurement principle in use; for underwater inertial navigation this is typically either a low-cost gyroscope aided by a magnetic compass to improve long-term stability or a gyrocompass capable of directly measuring Earth's rotation [23]. The former is cheaper, but is susceptible to deviation in the local magnetic field, solar winds, and self-induced magnetic variations due to varying electrical currents. A gyrocompass is not as susceptible to external influences, but the presence of gyro bias causes drift in the heading over time. For high-end INS the DVL induced position error is close to a magnitude larger than that of the accelerometers and gyroscopes for straight-line trajectories [24]. The performance of a gyroscope can be specified by its angular random walk (ARW) and bias instability. The former appears as additive zero-mean noise on the measured angular rates, and the latter as a bias varying at low frequencies [25]. The bias can be modeled as a zero-mean first order Gauss-Markov process in which its values are exponentially correlated with its past values, i.e. colored noise. In the Kalman filter, which only supports white (uncorrelated) noise directly, it is common to augment the state vector by additional states purely driven by noise to obtain the desired frequency characteristics [26]. In this work, dynamic states are avoided in order to derive analytical expressions for the steady-state covariance, which proves useful in solving the path planning problem. For this reason, the following approximation is applied for the uncertainty a gyrocompass [22].

$$\begin{aligned} \sigma_{\delta\psi} &= \sigma_{\delta\psi,\mathrm{IMU}} + \sigma_{\delta\psi,\mathrm{DVL}} \\ &\approx \frac{\Delta\omega}{\omega_{IE} \cos\mu} + \frac{\delta v}{u} \end{aligned} \tag{6}$$

Here, $\Delta\omega$ is the bias stability per specifications, $\omega_{IE} = 7.2921 \times 10^{-5}$ rad/ sec is the rotation rate of Earth relative to the inertial frame, and μ is the latitude taken to be 45 deg. The second term is an induced heading error by the DVL across-track error relative to the surge speed. Since we assume no nominal velocity in the across-track direction, this is taken to be the constant part of the DVL long-term accuracy specification. The nominal surge speed, u, is taken to be 2.0 m/s.

Take the matrix $\boldsymbol{Q}$ to mean the body-fixed velocity covariance matrix.

$$\boldsymbol{Q} = \begin{bmatrix} \sigma_x^2 & 0 \\ 0 & \sigma_y^2 \end{bmatrix} = \begin{bmatrix} \sigma_{\delta u}^2 & 0 \\ 0 & \sigma_{\delta v}^2 + u\sigma_{\delta\psi}^2 \end{bmatrix} \tag{7}$$

The time-derivative of the north-east covariance $\dot{\boldsymbol{P}}$ can then be represented as the projection of the body-fixed linear velocity errors onto the north-east axes provided that the true heading is known. The projection can be represented by a two-dimensional rotation matrix, $\boldsymbol{G}(t) = \boldsymbol{R}_2(\psi(t))$.

$$\dot{\boldsymbol{P}}^{\{n\}} = \mathrm{Cov}\left\{ \boldsymbol{G}(t) \begin{bmatrix} \delta u \\ \delta v + \delta\psi u \end{bmatrix} \right\}$$

$$= \boldsymbol{G}(t)\,\mathrm{Cov}\left\{\begin{bmatrix}\delta u\\ \delta v + \delta\psi u\end{bmatrix}\right\}\boldsymbol{G}^T(t)$$
$$= \boldsymbol{G}(t)\boldsymbol{Q}\boldsymbol{G}^T(t) \tag{8}$$

This time-varying equation can be integrated exactly for the case of constant turn rate, $\dot{\psi} = r$ with $\dot{r} = 0$. This is given by

$$\boldsymbol{P}_{t_0+\tau} = \boldsymbol{P}_{t_0} + \begin{cases}\boldsymbol{f}_r(\tau) - \boldsymbol{f}_r(0) & \text{for } r \neq 0\\ \boldsymbol{G}(t_0)\boldsymbol{Q}\boldsymbol{G}^T(t_0)\tau & \text{otherwise}\end{cases} \tag{9}$$

where

$$\boldsymbol{f}_r(\tau) = \begin{bmatrix}-s_{2\psi} & 2c_\psi^2\\ 2c_\psi^2 & s_{2\psi}\end{bmatrix}\frac{\sigma_y^2 - \sigma_x^2}{4r} + \frac{(\sigma_x^2 + \sigma_y^2)\tau}{2}\boldsymbol{I}_2$$

and $\psi = \psi_0 + r\tau$. If the variances along the body axes are identical, i.e. $\sigma_x^2 = \sigma_y^2$, the above reduces to $\boldsymbol{P}_{t_0+\tau} = \boldsymbol{P}_{t_0} + \tau\sigma^2\boldsymbol{I}_2$.

D. USBL ACOUSTIC POSITIONING

The position of the vehicle is estimated based on the measured acoustic range and direction. The range can be obtained from time-of-flight measurements based on one-way or two-way ranging. The direction of the wavefront can be measured by the phase shift of the incoming signals measured in a baseline formed by several transducers. With these measurements being known, the position of the target in the NED frame can be computed. The acoustic direction and range is taken to correspond to the direct path to the vehicle, i.e. that ray-bending has already been corrected for. The position of the ship is given by $\boldsymbol{p}_S^{\{n\}}$, and the mounting offset of the USBL system in the body frame is given by $\boldsymbol{p}_U^{\{b\}}$. With the range expressed in vector form as $\boldsymbol{r}^{\{u\}} = \begin{bmatrix}0, 0, r\end{bmatrix}^T$ and the measured bearing and elevation given by α and β respectively, the position of the target vehicle can be calculated as follows.

$$\boldsymbol{p}_{\mathrm{T}}^{\{n\}} = \boldsymbol{p}_S^{\{n\}} + \boldsymbol{R}_b^n(\boldsymbol{\Theta})\left[\boldsymbol{p}_U^{\{b\}} + \boldsymbol{R}_u^b(\alpha, \beta)\boldsymbol{r}^{\{u\}}\right] \tag{10}$$

Since the range in vector form is expressed along the z-axis of the USBL-frame ($\{u\}$), the measurement can be related to the body frame through the following rotation $\boldsymbol{R}_u^b(\alpha, \beta) = \boldsymbol{R}_{z,\alpha}\boldsymbol{R}_{y,\beta}$. The bearing and elevation measurements are assumed to be aligned with the body axes of the ship but can trivially be rotated from a different frame if necessary. The measurement uncertainties present in the acoustic range, acoustic direction, and ship attitude are assumed to be adequately described as zero-mean additive white noise. Since Gaussian distributions are only valid under linear transformations, the propagated uncertainty is approximated based on a first-order Taylor expansion of (10).

$$\mathrm{Cov}\left\{\boldsymbol{p}_T^{\{n\}}\right\} \approx \boldsymbol{J}_U\boldsymbol{\Sigma}\boldsymbol{J}_U^T \tag{11}$$

where $\boldsymbol{J}_U$ is the Jacobian with respect to the non-deterministic variables and $\boldsymbol{\Sigma}$ is the associated covariance matrix. This is a reasonable approximation for modest angular uncertainties. For larger angular uncertainties the projected probability distribution becomes curved and is no longer accurately described through linearization. While it is tempting to compute the partial derivatives with respect to the variables in (10) directly, the derivatives with respect to the spherical coordinate parametrization of the bearing and elevation does not necessarily reflect the physical uncertainty in the directional measurement. In the zy-parametrization there is a singularity along the z-axis, i.e. $\beta = 0$. Here, the partial derivative with respect to the z-rotation becomes zero and gives no net contribution to the measurement uncertainty along the y-axis. Instead, we want to represent a perturbation in the direction of the incoming wavefront, such that the directional uncertainty forms a cone towards the target irrespective of direction. We therefore make the following modification to the parametrization of the body-USBL rotation matrix.

$$\boldsymbol{R}_u^b(\alpha, \beta, \delta_1, \delta_2) = \boldsymbol{R}_{z,\alpha}\boldsymbol{R}_{y,\beta}\boldsymbol{R}_{y,\delta_2}\boldsymbol{R}_{x,\delta_1} \tag{12}$$

Here $\delta_1 \sim \mathcal{N}(0, \sigma_{\delta_1}^2)$ and $\delta_2 \sim \mathcal{N}(0, \sigma_{\delta_2}^2)$ are zero-mean perturbed angles about the direction of the incoming wavefront. The rotation to body frame according to the bearing and elevation is then performed as before, under the assumption that there is no uncertainty in these parameters. In this work, we apply these equations in a forward simulation, where this is always the case since the (unbiased) mean position of the underwater vehicle is known.

The partial derivative with respect to the angle of a rotation matrix can be calculated as the product of a skew symmetric matrix and the rotation matrix. The derivative with respect to the Euler angle ϕ about the x-axis can for example be computed as follows, where the coordinate frames have been omitted for brevity.

$$\frac{\delta \boldsymbol{p}_T}{\delta\phi} = \boldsymbol{R}_{z,\psi}\boldsymbol{R}_{y,\theta}S(\hat{\mathbf{i}})\boldsymbol{R}_{x,\phi}\left[\boldsymbol{p}_U + \boldsymbol{R}_u^b\boldsymbol{r}\right] \tag{13}$$

The partial derivatives can similarly be computed for the other variables. The full Jacobian of (10) can then be computed with respect to $\boldsymbol{x} = [\phi,\ \theta,\ \psi,\ \delta_1,\ \delta_2,\ r]^T$. These are the Euler angles of the ship, acoustic perturbation and acoustic range respectively. The uncertainty in the position of the ship is omitted as its already in the NED frame, and is constant no matter where the surface vessel is positioned.

$$\boldsymbol{J} = \begin{bmatrix}\frac{\partial p_{T,n}}{\partial\phi} & \cdots & \frac{\partial p_{T,n}}{\partial r}\\ \frac{\partial p_{T,e}}{\partial\phi} & \cdots & \frac{\partial p_{T,e}}{\partial r}\\ \frac{\partial p_{T,d}}{\partial\phi} & \cdots & \frac{\partial p_{T,d}}{\partial r}\end{bmatrix} \tag{14}$$

The Jacobian can be simplified by taking the roll and pitch to be zero, as the forward simulation does not include these degrees of freedom. Note that the uncertainty in the surface vessel pitch and roll is still propagated along the direction of the USBL measurement. If the body coordinate frame is additionally taken to be centered on the USBL, it can be simplified further. Under the assumptions above, the following Jacobian in NED can be derived for the Euler angles,

directional perturbation, and range respectively.

$$\boldsymbol{J}_U = \begin{bmatrix} rs_\psi c_\beta & -rc_\psi c_\beta & rs_\alpha s_\beta \\ rc_\psi c_\beta & rs_\psi c_\beta & -rc_\alpha s_\beta \\ -rs_\beta s_{\alpha+\psi} & rs_\beta c_{\alpha+\psi} & 0 \\ rs_{\alpha+\psi} & -rc_{\alpha+\psi} & 0 \\ rc_\beta c_{\alpha+\psi} & rc_\beta s_{\alpha+\psi} & -rs_\beta \\ s_\beta c_{\alpha+\psi} & s_\beta s_{\alpha+\psi} & c_\beta \end{bmatrix}^T \tag{15}$$

Assuming independence between the variables, the vector $\boldsymbol{x}$ may be described by a multivariate Gaussian distribution with a diagonal covariance matrix.

$$\boldsymbol{\Sigma} = \text{diag}(\sigma_\phi^2, \sigma_\theta^2, \sigma_\psi^2, \sigma_{\delta_1}^2, \sigma_{\delta_2}^2, \sigma_r^2) \tag{16}$$

Equation (11) can now be used to calculate the approximate propagated measurement uncertainty. This will be used to evaluate the reduction in uncertainty for the path planning.

E. DISCRETE-TIME USBL UPDATE VARIANCE

At each acoustic position update the prior belief of the underwater vehicle position can be fused with the measurement. The prior distribution can be taken to be the uncertainty at the last USBL negotiation plus the increase in uncertainty between the updates, calculated by (9). The measurement uncertainty is taken to be described by the linearized approximation in (11). The posterior distribution can then be computed based on Bayes theorem. Since both the prior and measurement distributions are taken to be multivariate Gaussian, the posterior probability distribution is given by the scaled product of two Gaussian probability density functions. This result is another Gaussian distribution, as it is conjugate to itself. The variance of the posterior is equal to the reciprocal sum of the reciprocal of the variances [27].

$$\begin{aligned} \boldsymbol{\Sigma} &= (\boldsymbol{\Sigma}_1^{-1} + \boldsymbol{\Sigma}_2^{-1})^{-1} \\ &= \boldsymbol{\Sigma}_1 \boldsymbol{\Sigma}_1^{-1} (\boldsymbol{\Sigma}_1^{-1} + \boldsymbol{\Sigma}_2^{-1})^{-1} \boldsymbol{\Sigma}_2^{-1} \boldsymbol{\Sigma}_2 \\ &= \boldsymbol{\Sigma}_1 (\boldsymbol{\Sigma}_1 + \boldsymbol{\Sigma}_2)^{-1} \boldsymbol{\Sigma}_2 \end{aligned} \tag{17}$$

The Sherman-Morrison-Woodbury inverse matrix modification formula can then be used to transform this equation into the following [28].

$$\begin{aligned} \boldsymbol{\Sigma} &= (\boldsymbol{\Sigma}_1^{-1} + \boldsymbol{\Sigma}_2^{-1})^{-1} \\ &= \boldsymbol{\Sigma}_1 - \boldsymbol{\Sigma}_1 (\boldsymbol{\Sigma}_1 + \boldsymbol{\Sigma}_2)^{-1} \boldsymbol{\Sigma}_1 \end{aligned} \tag{18}$$

This is in fact equivalent to the Kalman filter error covariance update equation; the minimum mean-square error estimator for linear-Gaussian systems. Inserting for the prior distribution and the measurement uncertainty yields the following expression for the posterior horizontal uncertainty conditioned on the measurement.

$$\boldsymbol{P}_{k+1} = \boldsymbol{P}_k^+ - \boldsymbol{P}_k^+ \left(\boldsymbol{P}_k^+ + \boldsymbol{R}_{d,k} \right)^{-1} \boldsymbol{P}_k^+ \tag{19}$$

Here, $\boldsymbol{R}_d = \boldsymbol{J}_{U,k} \boldsymbol{\Sigma}_k \boldsymbol{J}_{U,k}^T$ is the linearized measurement covariance as derived in the previous section. The prior covariance, $\boldsymbol{P}_k^+$, is given by (9). For an AUV following a straight path this is given by $\boldsymbol{P}_k^+ = \boldsymbol{P}_k + \boldsymbol{G}(\psi_k) \boldsymbol{Q} \boldsymbol{G}^T(\psi_k) \tau$. The attained reduction in variance by positioning the ASV at a series of locations can now be estimated, provided that the acoustic negotiation is successful.

The steady-state covariance can be calculated by taking the measurement Jacobian, update rate, and uncertainty increase between updates to be fixed in time. The expression for the steady-state covariance is derived in Appendix A, and restated below.

$$\boldsymbol{P}_{d,\infty} = \boldsymbol{Q}_d \left[\left(\boldsymbol{Q}_d^{-1} \boldsymbol{R}_d + \frac{1}{4} \boldsymbol{I} \right)^{\frac{1}{2}} - \frac{1}{2} \boldsymbol{I} \right] \tag{20}$$

Here, $\boldsymbol{Q}_d$ is the covariance increase between USBL measurements. The principal square root is used, for which every eigenvalue has a non-negative real value. This square root is unique for positive semi-definite matrices.

The steady-state standard deviation evaluated on a square grid of horizontal offsets is presented in Fig. 2 with the AUV fixed at the center at 100 m depth. If the body-fixed velocity errors are identical, the steady-state covariance in the north and east directions are the same, except rotated 90°. Moving along the east or north axes causes the steady-state covariance to remain low along the respective axis. The reason for this can be explained by considering a measurement with the target at the surface. The projected angular measurement uncertainty is then decomposed along the z-axis and the orthogonal direction in the horizontal plane. The projected uncertainty in the direction of the target is fully defined by the range uncertainty. In this work, we assign constant variance to the range measurement regardless of distance to the target. In practice the range uncertainty can vary slightly according to the signal strength (dB). We compensate for this by using a conservative value for the range uncertainty.

Using the steady-state covariance, the measurement covariance performed at a different update-rate can be calculated. This measurement is equivalent in a steady-state sense, but may deviate if there are strong transients. This will be used in the path planning to effectively decouple the problem formulation from the true rate of the measurements.

$$\boldsymbol{R}_z(\infty) = \boldsymbol{P}_{d,\infty} \boldsymbol{Q}_z^{-1} \boldsymbol{P}_{d,\infty} + \boldsymbol{P}_{d,\infty} \tag{21}$$

An example of the posterior covariance with USBL updates at different rates is shown in Fig. 3. There, an ASV and AUV pass across each other in a straight line along the east-west axis, with the AUV at a fixed depth. Note that both the body-fixed velocity uncertainty and measurement uncertainty have been increased relative to the other simulations to produce transients.

F. TRAJECTORY PLANNING

In this section, we formulate an optimal control problem (OCP) for the trajectory planning with USBL aiding. The OCP is implemented as a NLP through a direct multiple shooting approach. Direct methods discretize the control problem into time intervals called shooting intervals prior to optimizing and solves each sub-problem separately. Continuity along the solution trajectory is ensured by equality

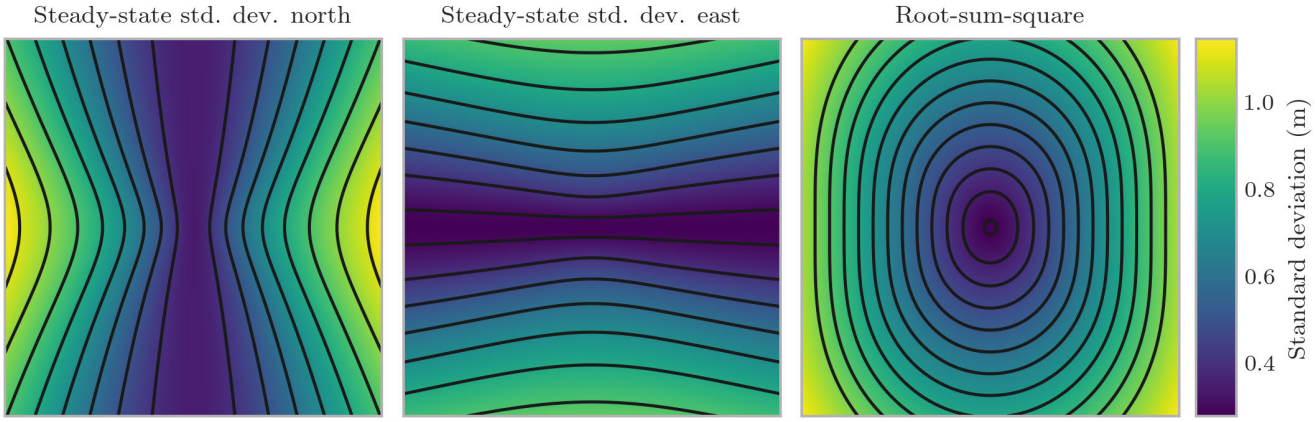

FIGURE 2. Steady-state standard deviation for an AUV at 100 meters depth, with a varying horizontal offset in north and east from -1000 m to 1000 m. The figures from left to right are; the steady-state uncertainty in north, east and root-sum-square, $\sqrt{\sigma^2_{N,\infty} + \sigma^2_{E,\infty}}$, of the two. At the center of the figures, the ASV is positioned directly on top of the AUV, causing a minima along both axes. Both the ASV and AUV are headed north. The isolines are spaced at 0.1 m intervals.

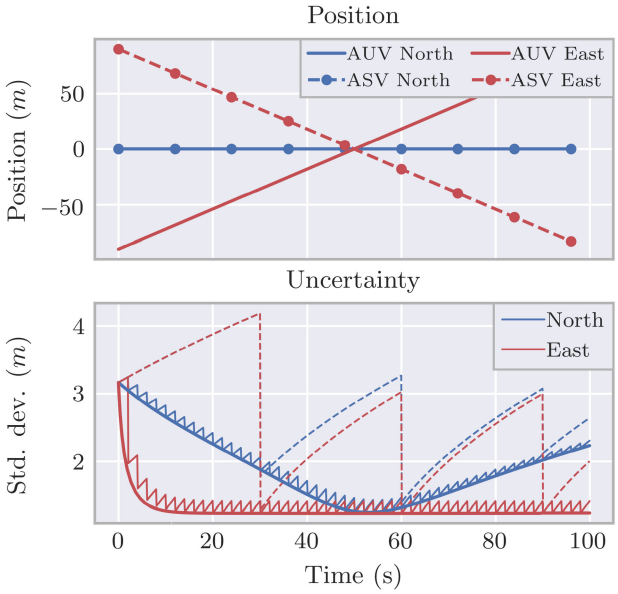

FIGURE 3. Comparison of the USBL update equation at different update rates using a modified measurement covariance based on the steady-state covariance. The AUV and ASV crosses on a straight path along the east axis, with the AUV remaining at a depth of 50 m throughout. The true USBL updates (2 s) are shown as small zig-zag lines, the dashed lines are modified measurements at 30 s intervals. The solid lines are steady-state equivalent continuous covariance updates solved using implicit Runge-Kutta 5 (see Appendix B).

constraints in the NLP. In our formulation, every shooting node has free decision variables, which is referred to as full discretization [29].

The multiple shooting approach considers both the control inputs and states to be decision variables. This results in a problem with a larger size and more degrees of freedom, but less nonlinear dependency on the control inputs. This improves the convergence for nonlinear problems as well as the numerical stability [30]. Since the states are taken to be decision variables, an initial guess can also be provided to speed up the convergence. A moving horizon approach is used, where the problem is solved over a finite time horizon. After solving, the horizon is shifted into the future, and warm-started using the previous solution. The prediction horizon is partitioned into n_p shooting intervals $[t_k, t_k + \tau], 0 \leq k \leq n_p$. Here, τ is the time step, i.e. the duration of the shooting interval. The inputs, surge velocity and turn rate, are taken to be piecewise constant on each interval $\boldsymbol{\nu}_S(t) = \boldsymbol{q}_k = (u_s, r_s)_k$. An initial value problem (IVP) is solved on each shooting interval to compute the response in position and heading.

$$\dot{\boldsymbol{x}}_k(t) = f_k(\boldsymbol{x}_k, \boldsymbol{q}_k), \quad \boldsymbol{x}_k(t_k) = \boldsymbol{s}_k \tag{22}$$

Here, s_k are the states at the shooting interval boundaries. The initial values of each interval are constrained to be equal to the solution of the previous interval. In this work, the kinematic IVPs are solved through an explicit Runge-Kutta order 4 (RK4) numerical integration. An exact integration was attempted but found to converge slower than RK4 with a negligible increase in accuracy.

The covariance of each AUV is propagated according to (19). Let the matrix $\boldsymbol{P}_{k,j}$ be the covariance at the beginning of shooting interval k, where $j \in \{1, \ldots, n_t\}$ denotes the target. Two formulations are considered. The first formulation assumes that all vehicles are ranged at equal rates throughout the shooting horizon. In that case, the nominal USBL rate is reduced according to the number of vehicles being tracked. The second formulation only ranges a single vehicle per shooting horizon. Binary decision variables are introduced, turning the formulation into a mixed-integer nonlinear program (MINLP). The binary decision variables $b_{k,j} \in \{0, 1\}$ are used to select the vehicle to range over each shooting interval. An inequality constraint is added to allow ranging to at most a single vehicle at a time (25h). Using an inequality instead of an equality allows for the option of ranging none

of the vehicles. This may for example occur if an energy cost is added when the USBL system is active. This aspect is not considered here, and ranging a vehicle is never considered negative, no matter how high the measurement covariance becomes.

$$\boldsymbol{P}_{k+1,j} = \boldsymbol{P}^+_{k,j} - b_{k,j}\boldsymbol{P}^+_{k,j}\left(\boldsymbol{P}^+_{k,j} + \boldsymbol{R}_{d,k,j}\right)^{-1}\boldsymbol{P}^+_{k,j} \tag{23}$$

Let the vector $\boldsymbol{c}_{k,j}$ represent the flattened covariance matrix for each target j, at the beginning of each shooting interval k. The states of the NLP at each shooting node are then taken to be described by the following vector.

$$\begin{aligned}\boldsymbol{s}_k &= \left[\boldsymbol{\eta}_k; \boldsymbol{c}_k\right] \\ &= \left[\boldsymbol{\eta}_k; \boldsymbol{c}_{k,1}; \ldots; \boldsymbol{c}_{k,n_t}\right]\end{aligned} \tag{24}$$

The positions of the underwater vehicles are supplied as fixed parameters in the NLP given a known plan and forward simulation by integrating (2). The uncertainty increase over each shooting interval is pre-computed for each underwater vehicle with (9). The NLP and MINLP are summarized below. The last inequality is exclusive to the MINLP formulation.

$$\min_{s,q} \sum_{k=1}^{n_p} \left\{L_k(\boldsymbol{s}_k, \boldsymbol{q}_k)\right\} + V_\infty(\boldsymbol{s}_{n_p}), \tag{25a}$$

$$\text{s.t.} \tag{25b}$$

$$\boldsymbol{x}_0 = \boldsymbol{s}_0, \tag{25c}$$

$$\boldsymbol{F}_{RK4}(t_k, \boldsymbol{\eta}_k, \boldsymbol{q}_k) = \boldsymbol{\eta}_{k+1} \quad 0 \le k < n_p, \tag{25d}$$

$$\boldsymbol{F}_C(t_k, \boldsymbol{\eta}_{k+1}, \boldsymbol{c}_k) = \boldsymbol{c}_{k+1} \quad 0 \le k < n_p, \tag{25e}$$

$$\underline{\boldsymbol{q}}_k \le \boldsymbol{q}_k \le \bar{\boldsymbol{q}}_k \quad 0 \le k < n_p, \tag{25f}$$

$$\Delta\underline{u}_k \le u_k - u_{k-1} \le \Delta\bar{u}_k \quad 0 \le k < n_p, \tag{25g}$$

$$1 \ge \sum_{j=1}^{n_j} b_{k,j} \quad 0 \le k < n_p \tag{25h}$$

From top to bottom the constraints are; initial value constraint, shooting constraints $\boldsymbol{F}_{RK4}$ for the kinematic equations, shooting constraints $\boldsymbol{F}_C$ for the covariance equations, input constraints (surge and heading rate), surge rate of change constraint. The final inequality limits the number of targets that can be ranged simultaneously in a shooting horizon, which is only included in the MINLP formulation. The propagation of covariance only depends on the state at the end of each shooting interval, and not any intermediate values. This means that the Jacobian is evaluated given the position of the surface vessel and underwater vehicles at that time. It is possible to introduce intermediate shooting nodes to increase the resolution of the update rate of the propagated uncertainty without increasing the input space. Alternatively, the duration of the shooting intervals can be reduced, but constraining a number of adjacent intervals to have equal inputs in order to avoid increasing the dimensionality of the input space. The latter is known as input blocking or move blocking [31].

The objective to be minimized is defined as a sum over a function, $L_k(\boldsymbol{s}_k, \boldsymbol{q}_k)$, evaluated at the end of each shooting interval. The following objective function is used.

$$\begin{aligned}L_k(\boldsymbol{s}_k, \boldsymbol{q}_k) = \frac{1}{n_t}\sum_{j=1}^{n_t} \mathrm{Tr}\left\{\boldsymbol{P}_{k,j}(\boldsymbol{s}_k, \boldsymbol{q}_k)\right\} \\ + w_u u_k^3 + w_{du}(u_k - u_{k-1})^2 \\ + w_r r_k^2 + w_{dr}(r_k - r_{k-1})^2\end{aligned} \tag{26}$$

Here, the trace of the horizontal covariance matrices are minimized across all vehicles. The trace is equal to the sum of the eigenvalues of the covariance matrix, e.g. variance along the major and minor axis. In this work, the uncertainty across the vehicles are weighted equally, but one vehicle can easily be prioritized by adding a vehicle-dependent weight inside the summation. The term is normalized by the number of vehicles for consistency in tuning of vehicle parameters. The second line adds penalties on the surge inputs and the change in velocity. The third line adds penalties on the turn rate inputs and the change in turn rate. The surge penalty is intended to represent the energy required to maintain the speed, whereas the other three are introduced to prefer paths without excessive changes to heading or speed. The cube of surge velocity is used to quantify the effective horsepower, i.e. the power required to tow a ship overcoming its resistance. A coarse approximation can be described by the following expression in salt water [32].

$$P_e = 0.0697 C_t S V^3_{\text{knots}}\,[\text{kW}] \tag{27}$$

The coefficient S denotes the wetted surface area (m^2), and C_t is a resistance coefficient which typically varies with the speed-to-length ratio of the ship. In this work, we are operating in a low speed regime, and this is taken to be described as a constant w_u which also scales the penalty relative to the covariance in the objective function. A more realistic resistance coefficient can be specified through a regression model, providing that it is sufficiently smooth and convex. The efficiency of the propulsion system can also be considered. An alternative strategy could be to replace the kinematic ship model with a dynamical model and define the energy in terms of the work done by the actuators [33].

The function $V_\infty(\boldsymbol{s}_{n_p}, \boldsymbol{q}_{n_p})$ is a terminal cost computed at the end of the horizon. This is taken to be the average of the traces of the steady-state covariance matrices across all vehicles, computed at the end of the final shooting interval.

$$V_\infty(\boldsymbol{s}_{n_p}, \boldsymbol{q}_{n_p}) = \frac{w_\infty}{n_t}\sum_{j=1}^{n_j} \mathrm{Tr}\left\{\boldsymbol{P}_{\infty,j}(\boldsymbol{s}_{n_p}, \boldsymbol{q}_{n_p})\right\} \tag{28}$$

The use of a terminal cost has been well studied with respect to optimality and stability in finite horizon model predictive control [34]. In this work, the terminal cost has been found to improve convergence and path stability, especially for shorter planning horizons. In the MINLP formulation, the terminal cost is still taken to be the average steady-state variance across all vehicles, and not just the target being tracked,

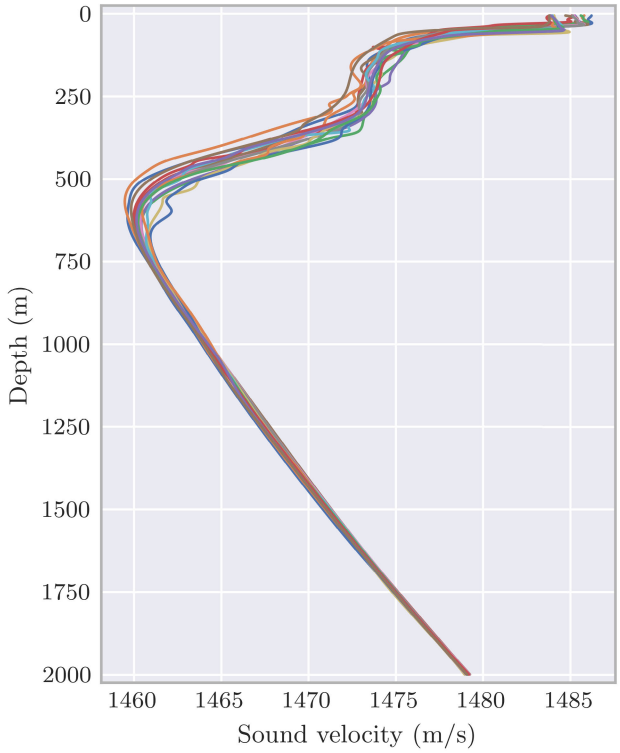

FIGURE 4. Sound velocity profiles (SVP) at the Arctic Mid-Ocean Ridge (AMOR) measured between August 22nd and September 1st of 2016. The SVPs are calculated based on conductivity, temperature, and depth (CTD) measurements onboard an AUV. The profiles have been fitted to splines but are not overly smooth and are representative of the raw measurements.

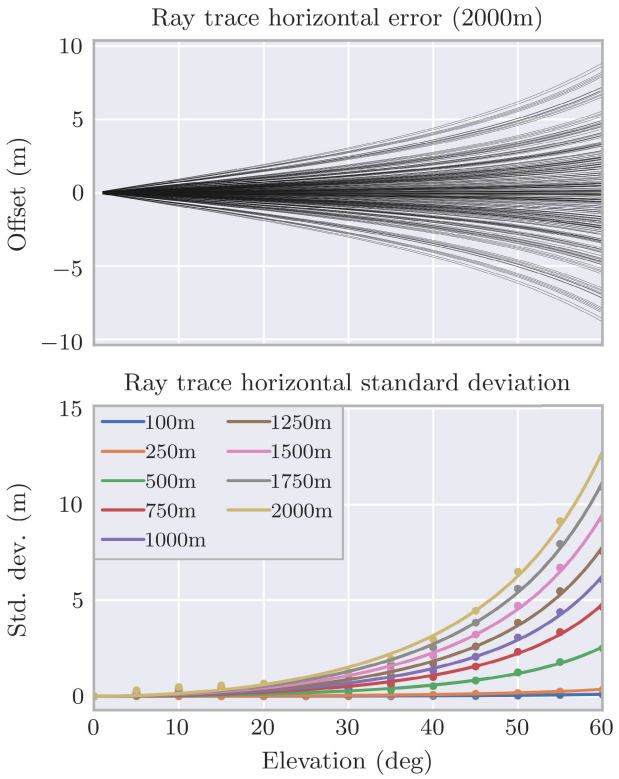

FIGURE 5. Horizontal errors resulting from ray trace using SVPs from Fig. 4. The horizontal errors have been calculated for each pair of profiles, where one is taken to be the true profile and the other is the one used by the USBL system. The first plot shows the errors at 2000 m, while the bottom plot shows standard deviations across a set of depths. The x-axis is the elevation directly to the true position. The circles in the bottom plot correspond to a third order polynomial fit of the standard deviations.

to encourage a position that is advantageous for all vehicles towards the end of the prediction horizon.

G. SOUND VELOCITY PROFILE

If the SVP is perfectly known, non-constant sound speed and ray-bending can be accounted for. The SVP can change over time or at different locations, however. Acoustic waves emitted directly at nadir are not ray-bended. For this reason, placing the surface vessel directly on top of the estimated horizontal position of the underwater vehicle is generally recommended. In this work, we want the topside vehicle to be able to deviate from that recommendation, and the induced errors must therefore be quantified in some way. The variation of the SVP is highly dependent on the location, season, and weather conditions. Actual profiles measured across the span of a week are therefore used as examples of possible variation in open ocean conditions. These profiles can be seen in Fig. 4. The profiles were measured at the Arctic Mid-Ocean Ridge (AMOR) in August/September of 2016 in approximately the same area. The BELLHOP ray trace software is used to compute the acoustic propagation for these profiles over a wide range of launch angles [35].

For each pair of SVP profiles, the first is taken to be the true profile and the second the one in use by the USBL system. The time of intersection by a specified depth layer in the true profile is found. The horizontal position at the same time for the same launch angle is then found in the ray trace for the USBL system. The horizontal offset between the true and measured profile can be seen in Fig. 5.

The x-axis is the elevation angle directly towards the true position of the underwater vehicle (without ray-bending). The upper plot is an example of the offsets at 2000 m for all pairs of profiles. The plot is symmetric about zero since the each pair is evaluated in both directions. The standard deviation of the horizontal error, plotted at multiple depths, can be seen in the lower plot. The horizontal errors are fitted to third order polynomials without the constant term at discrete depths. This expression is then used to penalize the horizontal distance to the underwater vehicle.

$$\sigma_h(r_h, z) = c_1(z)r_h + c_2(z)r_h^2 + c_3(z)r_h^3 \tag{29}$$

Adding depth as a regressor is possible, for example by assuming a linear sound velocity profile in the isothermal layer. The SVP error is added to the measurement uncertainty along the axis corresponding to the horizontal direction to the underwater vehicle.

$$\boldsymbol{R}_d = \boldsymbol{J}_U \boldsymbol{\Sigma} \boldsymbol{J}_U^T + \boldsymbol{R}_2(\psi + \alpha) \begin{bmatrix} \sigma_h^2 & 0 \\ 0 & 0 \end{bmatrix} \boldsymbol{R}_2^T(\psi + \alpha) \tag{30}$$

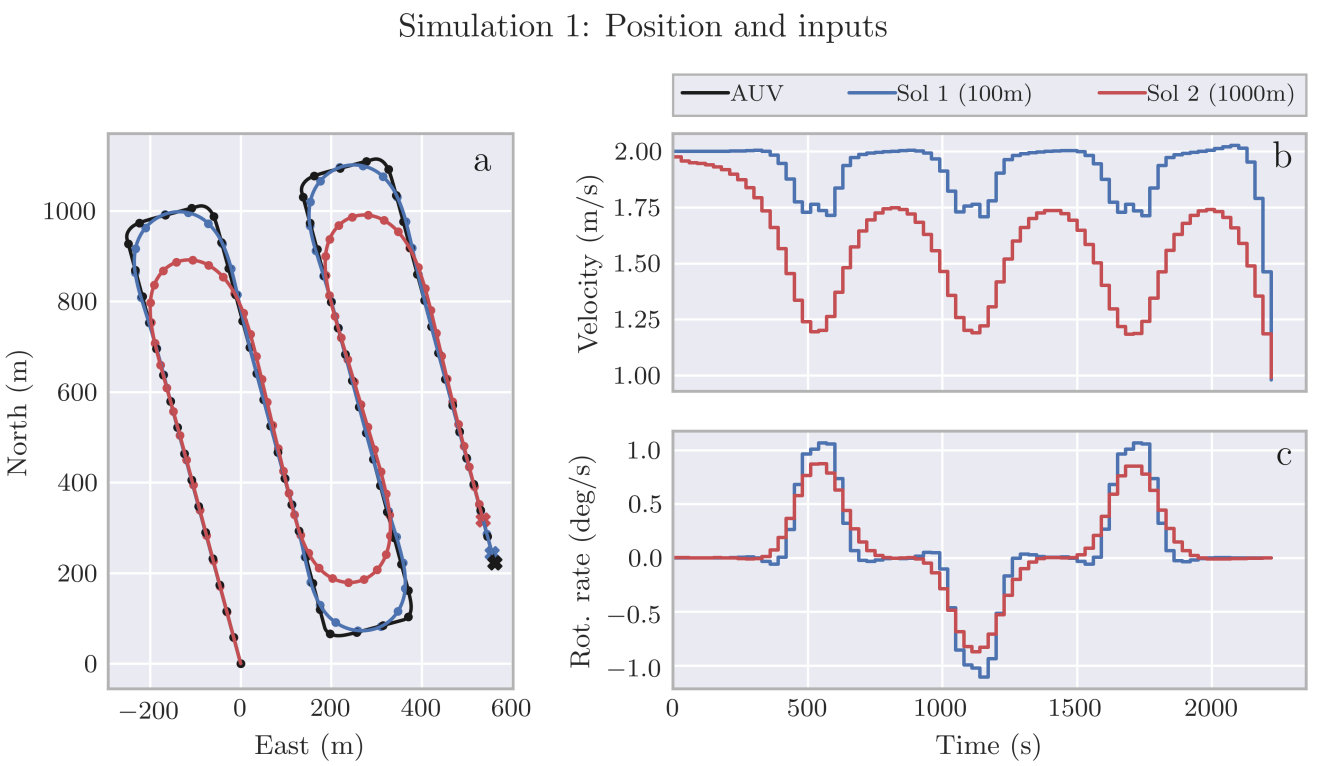

FIGURE 6. Position and inputs of simulation 1. The horizontal position of the AUV is plotted in black. The two ASV paths, in blue and red, are computed trajectories when the AUV is at 100 m and 1000 m respectively. The circles with the same colors corresponds to a shooting node in the NLP. At these locations, the Jacobian is evaluated in the NLP. The initial positions are (0, 0).

One benefit is that the current uncertainties about the north/east axes are taken into account when considering the SVP errors. The downside is that the SVP error is treated as zero-mean additive Gaussian noise, when in reality it is a systematic error. Increasing the measurement covariance will nonetheless discourage large elevation angles and have the effect we seek. The standard deviations are taken to be fixed in time. This is obviously not the case in a real setting, as the uncertainty will be low immediately after measuring the profile and become more uncertain as time goes on. In a practical implementation, the magnitude of the SVP error can be increased as a function of time since the last measurement to make the trajectories more conservative as time goes on.

III. SIMULATION

The methods presented so far are demonstrated through a series of simulations. The parameters for the uncertainties can be found in Table 1 and the NLP parameters in Table 2. The INS uncertainty is taken to be somewhere between a low-end and high-end system. This is done in order to have a tangible increase in the uncertainty of the targets within the planning horizon. Reasonable settings for the uncertainty may be obtained by measuring the position of the underwater vehicle on a straight-line trajectory without sending the measurements to the INS. The tuning of the NLP parameters was done by first setting the surge and yaw rate constraints to sensible values for a mid-sized craft and tuning the surge penalty to generate sensible trajectories. The remaining parameters were then tuned to prefer trajectories with smooth turns and moderate changes in surge. The kinematic constraints should reflect the attainable performance of the underlying dynamical system. All simulations were performed using a moving horizon approach, where the trajectory was shifted forwards one step at each iteration. The solver was warm-started based on the solution at the previous iteration. The first iteration used a solution obtained by minimizing the horizontal distance to the targets.

TABLE 1. Uncertainty parameters.

Symbol	Unit	Value	Description
$\sigma_\phi, \sigma_\theta$	deg	0.05	Ship roll, pitch std.
σ_ψ	deg	0.5	Ship heading std.
$\sigma_{\delta_1}, \sigma_{\delta_2}$	deg	1.0	Acoustic angle std.
σ_r	m	0.5	Acoustic range std.
κ_{DVL}	-	0.012	AUV DVL scale factor
$\sigma_{\epsilon,\text{DVL}}$	m s^{-1}	0.006	DVL constant error std.
$\Delta\omega$	deg /h	0.03	IMU heading error
$\sigma_{\delta u}$	m s^{-1}	0.03	DVL along-track std.
$\sigma_{\delta v}$	m s^{-1}	0.003	DVL across-track std.
$\sigma_{\delta\psi}$	deg	0.4	AUV Heading std.

A. SIMULATION I: SINGLE UNDERWATER VEHICLE

The first scenario consists of a single underwater vehicle moving in a lawn-mover pattern, a pattern commonly used

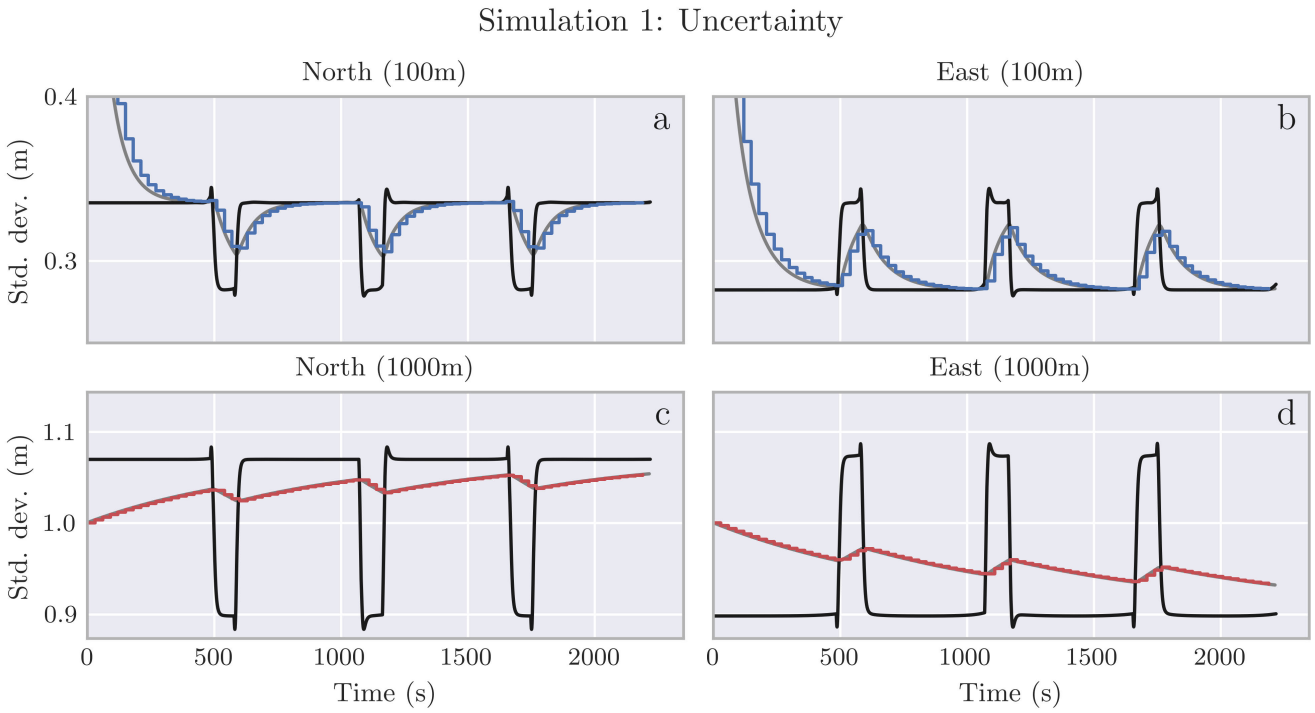

FIGURE 7. Standard deviations for simulation 1. The top figures and bottom figures are for the AUV at 100 m and 1000 m respectively (blue, red). The gray lines are USBL updates performed at the true USBL update rate (5 s) and the black lines are the steady-state standard deviations calculated at that exact point.

TABLE 2. NLP parameters.

Symbol	Unit	Value	Description
τ_{USBL}	s	5	True USBL update rate.
τ_z	s	30	Simulated USBL update rate.
$u_{\min}$	m s^{-1}	0.0	Surge, min. lim.
$u_{\max}$	m s^{-1}	5.0	Surge, max. lim.
Δu	m s^{-1}	0.025	Surge rate of change lim.
$r_{\min}$	deg /s	-2.0	Yaw rate, min. lim.
$r_{\max}$	deg /s	2.0	Yaw rate, max. lim.
w_u	–	0.0005	Surge cubic penalty weight
w_r	–	1.5	Rot. rate penalty weight
w_{du}	–	0.01	Surge diff. penalty weight
w_{dr}	–	10	Rot. rate diff. penalty weight
w_∞	–	$0.2n_p$	Terminal constraint weight

in seabed surveys. The scenario is simulated twice; once for an AUV at 100 m depth, and once for an AUV at 1000 meters depth. Since only one vehicle is being tracked, the MINLP formulation is not considered. The position and inputs of the two simulations can be seen in Fig. 6. The two paths differ in the turns. The reason for this is that the angular uncertainties increase with range. A horizontal displacement directly affects the range more at smaller depths. A consequence of this is that the surface vessel can cut the corner more while tracking the deeper underwater vehicle, with a negligible increase in the measurement covariance.

The estimated standard deviations for both simulations can be seen in Fig. 7. The upper plots are the north-east standard deviations at 100 m, and the plots on the bottom are for the AUV at 1000 m. The gray lines are the standard deviations for updates performed at the true update rate (5 s). The black lines are the steady-state standard deviations calculated at each position. The fluctuations are dominated by the change in heading of the underwater vehicle, as the forward surge uncertainty is larger than the sway uncertainty. The spikes in the steady-state standard deviation occurs because the AUV turns past the north/east axis, causing a maximum when aligned with the axis.

B. SIMULATION II: MULTIPLE UNDERWATER VEHICLES

Here we consider a multi-tracking objective with two underwater vehicles. Both vehicles have the same parameters and maintains the same speed ($2.0\,\text{m s}^{-1}$) and depth (150 m) throughout the simulation. Three trajectories for surface vessels are generated and is presented in Fig. 8 along with the computed inputs. The crosses indicate the end of each trajectory. The first trajectory (blue) is generated based on an objective function that only takes the sum of steady-state variances for both vehicles into account at every step. Since both targets are at the same depth, this trajectory follows the horizontal mid-point between them. This trajectory is used as a base-case. The second trajectory is generated based on the NLP formulation (red). The third trajectory is based on the MINLP formulation (cyan). The colors of the circles indicate which underwater vehicle was ranged in the previous shooting horizon. As expected, the MINLP formulation results in a trajectory that is more focused towards one vehicle at a time

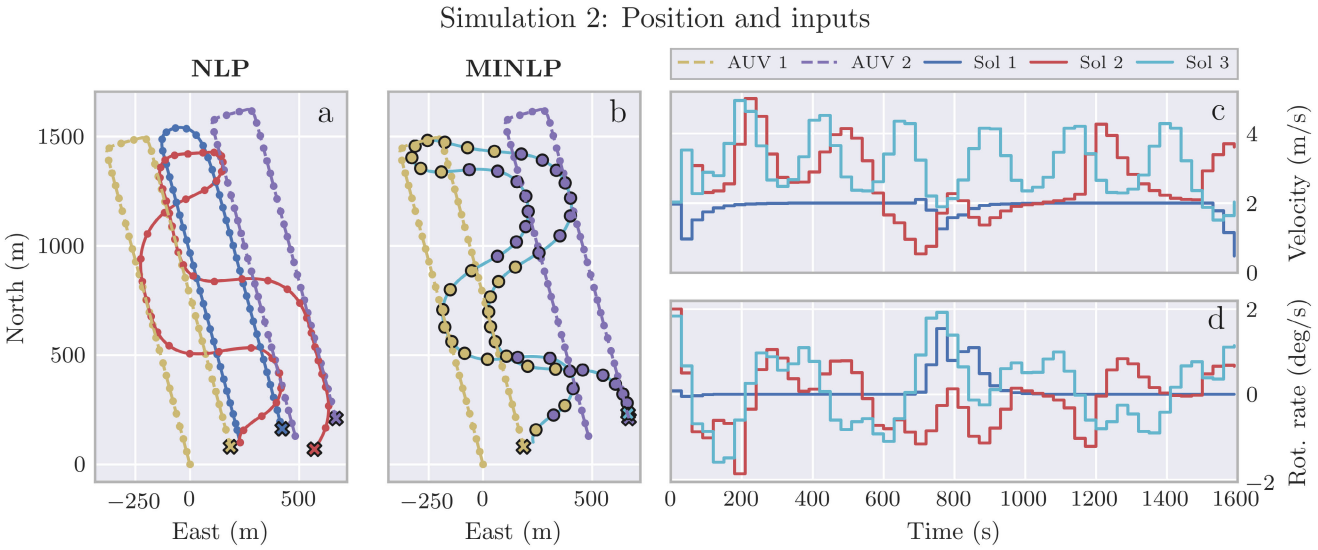

FIGURE 8. Position and inputs of simulation 2. The dashed lines are the horizontal positions of the AUVs, both at 150m depth throughout the simulation. The trajectory labeled as ASV 1 (blue) is the path planned by only considering the steady-state covariance at each step. The trajectories labeled as ASV 2 (red) and ASV 3 (cyan) are paths planned by considering the covariance along the trajectory with the steady-state covariance as a terminal cost. The circles with the same colors corresponds to a shooting node in the NLP. The crosses mark the end of the simulation for each path.

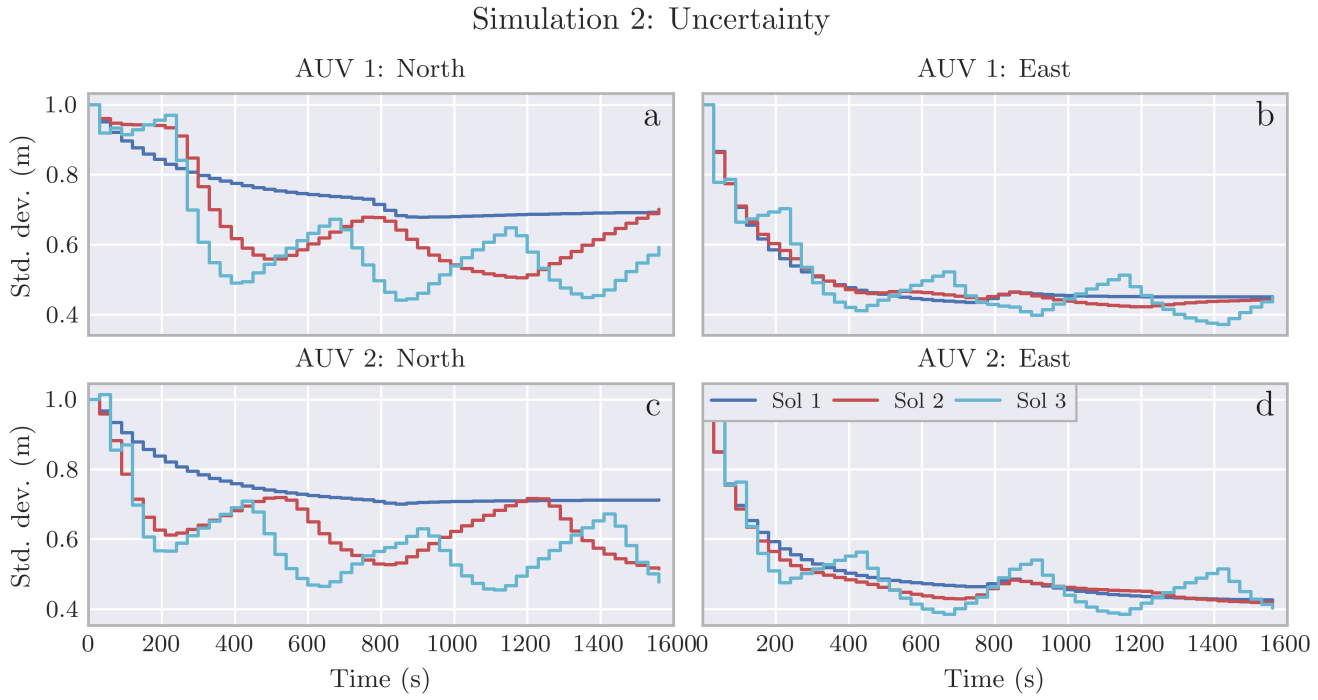

FIGURE 9. Standard deviations for simulation 2. The top figures and bottom figures are for the first and second AUV, respectively.

and utilizes more surge input to alternate between the two. The NLP on the other hand must track each vehicle longer before switching since the update rate per vehicle is lower. This comes at a cost however, as the MINLP is inherently more difficult to solve. The computational requirements are compared in Section IV-B. The first solution is computed based on a look-ahead horizon of 60 s. The solution does not change for longer horizons. The last two trajectories are computed using a look-ahead horizon of 600 s.

The covariance for all three trajectories is presented in Fig. 9. The sum of variances across the entire solution is 134 m^2, 123 m^2, and 117 m^2 for the base-case, NLP, and MINLP solutions, respectively. The MINLP can capitalize on targeting a specific vehicle at a time.

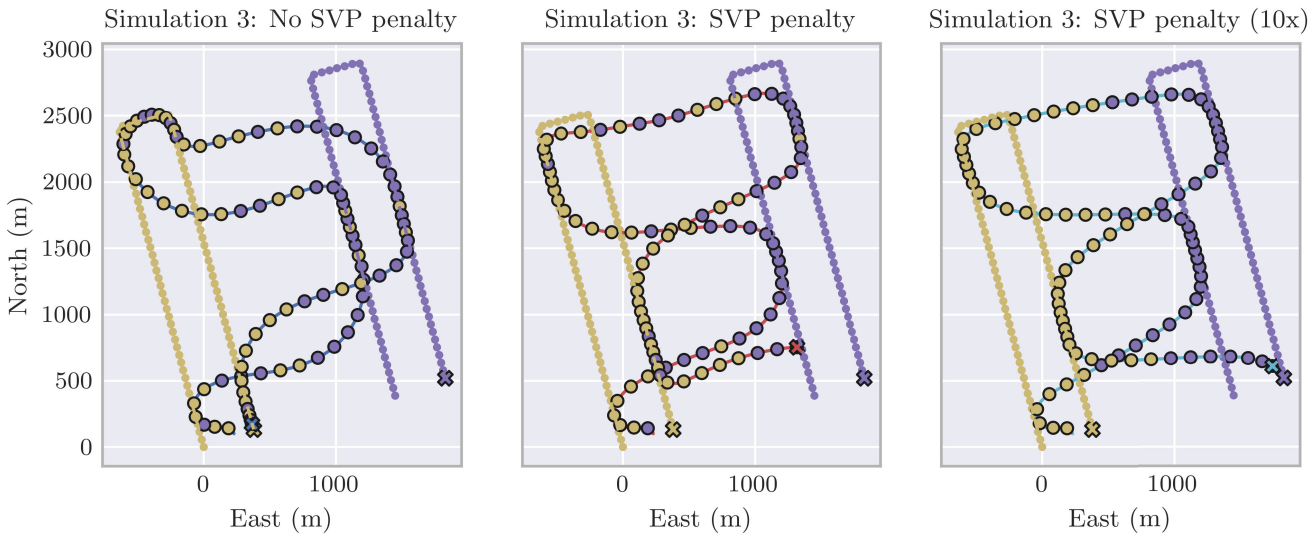

FIGURE 10. Position and inputs of simulation 3. Solution 1 (left) has no sound velocity error penalty. Solution 2 (middle) adds the SVP error to the measurement covariance of the target being tracked. Solution 3 (right) adds the SVP error to the measurement covariance of the target being tracked, except scaled 10 times.

C. SIMULATION III: SOUND VELOCITY ERRORS

In this simulation, the effect of the SVP penalty is investigated. The simulations so far have already added the sound velocity errors to the measurement covariance. The presented solutions have not been notably affected by this due to the small horizontal distances. In this simulation the length of the plan and distance between the targets have therefore been increased. The solutions are presented in Fig. 10.

Solution 1 (left) presents a trajectory without considering any SVP errors, as a reference. Solution 2 (middle) adds the SVP error to the measurement covariance of the target vehicle, as before. Solution 3 (right) also adds the SVP error to the measurement covariance but scales it 10 times. This is done to highlight the effects of an increased SVP error. The trajectory without the SVP penalty decides to occasionally range from one side to the other, and therefore only moves across twice. When the SVP penalty is added, the solution moves across a third time at the end. For the second trajectory, there is still some benefit to ranging across, whereas for the scaled SVP error this is no longer the case, instead focusing fully on the nearest target. The penalty is added on the horizontal axis corresponding to the direction of the ranging. This also provides some incentive to range in the direction of the minor axis of the target covariance matrix.

IV. DISCUSSION

A. LOCALIZATION AND TRACKING

This section links back to the scenarios outlined in Fig. 1. The focus in this work has been on solving the path planning problem with basis in the expected error growth for the target over time, calculated measurement uncertainty, and penalties on the control inputs. The localization problem has not been considered. In other words, the positions used throughout the simulations are deterministic. Since the onboard INS on the vehicle has access to high-rate inertial and velocity measurements in addition to the acoustic positioning, it will generally be able to estimate its position more accurately than an external observer. For this reason, it may be tempting to transmit the INS estimate over an acoustic link at regular intervals to reset the estimate onboard the surface vessel. One drawback of this is that it introduces a feedback loop between the INS system and surface vessel path. Consider an underwater vehicle and surface vessel moving in the same direction at some fixed horizontal offset. If the sound speed profile has a negative gradient, e.g. in a thermocline, the sound will be refracted downwards. This causes a systematic error in the horizontal position estimate towards the surface vessel. The INS estimate may therefore diverge from the true location, if the INS adjusts its position or bias estimates in response to the measurements. Although this is an extreme example, it illustrates the need to decouple the tracking from the INS of the target system. One possible approach is to use the INS estimate and progress along the plan to simulate the trajectory forwards in time, but shift the result corresponding to the observed offset from the USBL measurements. This can for example be realized by modeling the error state between the INS position and USBL measurement as a Gauss-Markov process. Since the acoustic waves cannot be bent past nadir, tracking the horizontal location of the acoustic position measurements is never a bad strategy. The pitch and heading of the underwater vehicle can be estimated based on the change in position and depth, but it is likely better to update these over an acoustic link.

B. PERFORMANCE

The mixed-integer problem is solved based on a branch-and-bound approach, and its efficiency depends on how quickly it is able to discard sub-optimal branches. Another

caveat with the MINLP is that each new target to track adds $n_p - 1$ new binary decision variables. The NLP formulation on the other hand does not increase the dimensionality of the input space for each new vehicle, only adding new shooting constraints. For tracking of a single vehicle, there is no reason to consider the MINLP formulation. The second simulation is used to quantify the computational requirements. On an Intel(R) Core(TM) i5-4670K @ 4.0GHz CPU, a single horizon of 600 s was on average computed in 0.004 s, 0.031 s, 0.065 per horizon for the base-case, NLP, and MINLP respectively. The MINLP took approximately twice as long to compute compared to the NLP. To evaluate the applicability for embedded use, the same simulation was also performed on a Raspberry Pi 3B with a 1.2GHz Broadcom BCM2837 ARMv8 CPU. The evaluation times are now on average 0.034 s, 0.31 s, 0.55 s per horizon. Although this nearly increases the computational times by 10x, the time it takes to solve for a single horizon is still well below a second on average. The surface vessel can compute the next horizon while executing the first step of the previous solution. Since the shooting intervals are 30 s, there should be enough computational headroom. Obviously, the solution times may depend on the paths of the targets and should only be used as an indication of the performance. The simulations were implemented in Python and can be re-implemented using the C++ CasADi interface or by using its code-generation utilities to further improve performance. Reducing the look-ahead horizon is an obvious way to tune performance but may impact the quality of the generated trajectories. The possibility of online re-planning is essential to account for uneven progress along the plan. Examples include varying bathymetry or unforeseen interruptions such as anti-collision behavior.

C. SCALABILITY

A conventional USBL scheme does not scale well with the number of underwater vehicles, as a message exchange is necessary to transmit the measured position to the vehicle. Using one-way travel time inverted-USBL is a possible solution if scalability is needed, as the range and direction can be calculated onboard each vehicle based on a broadcasted position from a the topside beacon at a known time [36], [37]. This requires synchronized clocks with high accuracy and USBL capability on each underwater vehicle, however.

The scalability also depends on the physical parameters of the surface vessel. The surface vessel may need to maintain a reduced speed, both due to the drag introduced by the protruding transceiver head and the formation of bubbles under the transceiver at higher speeds. If the transceiver head can physically retract into the hull, one may be able to maintain a higher speed whilst moving between vehicles. In any case, there is a physical limit to how many vehicles can reasonably be tracked simultaneously by a single surface vessel. How closely each vehicle needs to be tracked also depends on the quality of the onboard INS. A simulation where four vehicles are tracked with the MINLP formulation is shown in Fig. 11.

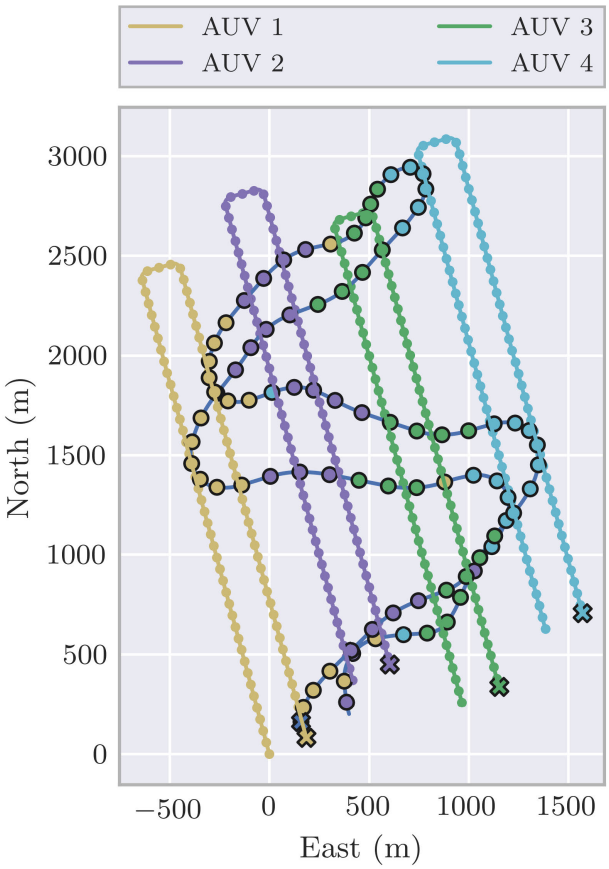

FIGURE 11. Trajectory generated for tracking of four vehicles at the same depth (150 m) and speed (2 ms^{-1}) using the MINLP formulation.

V. FUTURE WORK

The dropout rate of the acoustic communication and ranging is not taken explicitly into account in the planning problem. However, it is possible to set the initial covariance for the next horizon based on the actual number of successful position updates. While this may cause that target to be prioritized in the next horizon, it does not integrate the notion of a range-dependent error. Instead, the error rate may be modeled as a function of the signal strength (dB) or signal integrity. The signal strength can then be estimated online as a function of range, either from the acoustic measurements or by calculating the absorption in seawater based on CTD measurements. It is also possible to update the covariance from the INS system onboard the vehicles over an acoustic link. Multi-path propagation has not been considered, which may pose a problem especially in shallow water. It may be possible to position the surface vessel such that multi-path effects via the surface and seabed are minimized. This is difficult to include however, since the penalty would be dependent on the bathymetry and may introduce significant non-convexity in the optimization problem due to shadow-zones and caustics. The sound velocity errors have been treated as zero-mean additive noises. Although this penalizes large elevation angles, it does not consider

the cumulative effect of ranging along the same direction in the body frame of the target for prolonged periods. If the systematic offset in position always appears on the same side in the body-frame, erroneous biases may be estimated in the vehicle INS. While it is possible to design the survey pattern with this in mind, it may also be possible to add a state to the optimization problem that keeps track of the induced bias over time, and then seek to minimize this by either positioning the surface vessel on top of the vehicle or ranging from the opposite direction.

VI. CONCLUSION

In this work, a trajectory planning procedure has been presented for an autonomous surface vessel. The planned trajectories minimize the horizontal uncertainty for one or multiple underwater vehicles. The surface vehicle is assumed to be equipped with an ultra-short baseline transceiver capable of measuring the direction and range to the vehicles. The objective and constraints are formulated as an optimization problem. This is solved under the assumption that the movement of each vehicle is known within the planning horizon, e.g. by knowing the next waypoints. Two formulations are proposed, one where all vehicles are assumed to be ranged continuously, and one where an explicit decision of which vehicle to track is made. The latter has been found to provide better solutions in conventional ultra-short baseline setups for multiple vehicle tracking. The optimization problem has been found to be stable and quickly converge to a solution, even on an embedded system. The solution is thus suitable for real-time replanning in order to account for dropouts, uneven progress along the plan, or unforeseen interruptions.

APPENDIX A
STEADY-STATE COVARIANCE AND EQUIVALENT MEASUREMENT COVARIANCE

In this section, an expression for the steady-state covariance is derived. This result is subsequently used to compute a measurement covariance at a different sample-rate, which is equivalent at steady-state conditions. The discrete measurement covariance, $\boldsymbol{R_d} = \boldsymbol{J}_U \boldsymbol{\Sigma}_U \boldsymbol{J}_U^T$, is taken to be fixed in time. We take the matrix $\boldsymbol{Q}_d(\infty) = \int_0^\tau \boldsymbol{G}(\infty)\boldsymbol{Q}\boldsymbol{G}^T(\infty)dt$ to mean the increase in uncertainty between USBL updates at steady-state. Covariance matrices are only required to be positive semi-definite. In the following we require the covariance matrices, i.e. $\boldsymbol{P}_d$, $\boldsymbol{R}_d$, $\boldsymbol{Q}_d$, to be positive definite and thus non-singular and invertible. We now proceed with the discrete covariance update equation.

$$\boldsymbol{P}_{k+1} = \boldsymbol{R}_{d,k}(\boldsymbol{P}_k + \boldsymbol{Q}_{d,k} + \boldsymbol{R}_{d,k})^{-1}(\boldsymbol{P}_k + \boldsymbol{Q}_{d,k})$$

Since the covariance is at steady state, the update brings the covariance back to the same level as the previous update. We can therefore make the following substitution $\boldsymbol{P}_{k+1} = \boldsymbol{P}_k = \boldsymbol{P}$. Rearranging the equation above on the left-hand side gives the following quadratic matrix equation.

$$\begin{aligned}\left(\boldsymbol{P}_d + \boldsymbol{Q}_d + \boldsymbol{R}_d\right)\boldsymbol{R}_d^{-1}\boldsymbol{P}_d &= \boldsymbol{P}_d + \boldsymbol{Q}_d \\ \boldsymbol{P}_d\boldsymbol{R}_d^{-1}\boldsymbol{P}_d + \boldsymbol{Q}_d\boldsymbol{R}_d^{-1}\boldsymbol{P}_d - \boldsymbol{Q}_d &= \boldsymbol{0}\end{aligned}$$

We make the following algebraic manipulations to put the equations on a different form.

$$\begin{aligned}\left(\boldsymbol{P}_d + \boldsymbol{Q}_d\right)\boldsymbol{R}_d^{-1}\boldsymbol{P}_d &= \boldsymbol{Q}_d \\ \left[\left(\boldsymbol{P}_d + \boldsymbol{Q}_d\right)\boldsymbol{R}_d^{-1}\boldsymbol{P}_d\right]^{-1} &= \boldsymbol{Q}_d^{-1} \\ \boldsymbol{P}_d^{-1}\boldsymbol{R}_d\left(\boldsymbol{P}_d + \boldsymbol{Q}_d\right)^{-1} &= \boldsymbol{Q}_d^{-1} \\ \boldsymbol{P}_d\boldsymbol{Q}_d^{-1}(\boldsymbol{P}_d + \boldsymbol{Q}_d) - \boldsymbol{R}_d &= \boldsymbol{0} \\ \boldsymbol{P}_d\boldsymbol{Q}_d^{-1}\boldsymbol{P}_d + \boldsymbol{P}_d - \boldsymbol{R}_d &= \boldsymbol{0}\end{aligned}$$

The above is a quadratic matrix expression with coupled cross terms. The expression is similar to the algebraic Riccati equation. We left-multiply by $\boldsymbol{Q}_d^{-1}$ and define $\boldsymbol{Z} = \boldsymbol{Q}_d^{-1}\boldsymbol{P}_d$.

$$\begin{aligned}\boldsymbol{Q}_d^{-1}\boldsymbol{P}_d\boldsymbol{Q}_d^{-1}\boldsymbol{P}_d + \boldsymbol{Q}_d^{-1}\boldsymbol{P}_d - \boldsymbol{Q}_d^{-1}\boldsymbol{R}_d &= \boldsymbol{0} \\ \left(\boldsymbol{Q}_d^{-1}\boldsymbol{P}_d\right)^2 + \boldsymbol{Q}_d^{-1}\boldsymbol{P}_d - \boldsymbol{Q}_d^{-1}\boldsymbol{R}_d &= \boldsymbol{0} \\ \boldsymbol{Z}^2 + \boldsymbol{Z} - \boldsymbol{Q}_d^{-1}\boldsymbol{R}_d &= \boldsymbol{0}\end{aligned}$$

By completing the square, we can put the expression into the following form.

$$\left(\boldsymbol{Z} + \frac{1}{2}\boldsymbol{I}\right)^2 = \boldsymbol{Q}_c^{-1}\boldsymbol{R}_c + \frac{1}{4}\boldsymbol{I}$$

Which can be solved as follows.

$$\begin{aligned}\boldsymbol{Z} &= \left(\boldsymbol{Q}_d^{-1}\boldsymbol{R}_d + \frac{1}{4}\boldsymbol{I}\right)^{\frac{1}{2}} - \frac{1}{2}\boldsymbol{I} \\ \boldsymbol{P}_{d,\infty} &= \boldsymbol{Q}_d\left[\left(\boldsymbol{Q}_d^{-1}\boldsymbol{R}_d + \frac{1}{4}\boldsymbol{I}\right)^{\frac{1}{2}} - \frac{1}{2}\boldsymbol{I}\right]\end{aligned}$$

Note that in general, the square root of a matrix can have many possible solutions. Here, we refer to the principal square root, for which every eigenvalue has a nonnegative real value. This square root is unique for positive semi-definite matrices. Using the following expression, the measurement covariance at a different sample rate than the true rate can now be calculated.

$$\boldsymbol{R}_z(\infty) = \boldsymbol{P}_{d,\infty}\boldsymbol{Q}_z^{-1}\boldsymbol{P}_{d,\infty} + \boldsymbol{P}_{d,\infty}$$

Here, $\boldsymbol{R}_z$ and $\boldsymbol{Q}_z$ denotes the measurement covariance and increase in uncertainty between measurements respectively. The latter can be calculated by replacing the integration limits for $\boldsymbol{Q}_d(\infty)$. Obviously, these equations are based on steady-state conditions and may deviate if the covariance is in a transient phase, for example during initialization or if the measurement covariance suddenly changes. In this work, the measurement covariance changes as a function of a relatively slow-moving process, and has not been found to be an issue within the control horizon.

For the above to work the principal square root must exist, e.g. the operand must have positive eigenvalues. The inverse of a symmetric positive definite matrix is also symmetric positive definite [38]. The product of two symmetric positive definite matrices has positive eigenvalues [39]. The product of $\boldsymbol{Q}_d^{-1}$ and $\boldsymbol{R}_d$ therefore has positive eigenvalues, but is not

necessarily symmetric anymore. Adding a positive diagonal matrix only increases the eigenvalues. The principal square root therefore always exists for the above expression, provided that $\boldsymbol{Q}_d$ and $\boldsymbol{R}_d$ are positive definite. The principal root for non-singular square matrices can be computed based on the Schur decomposition of the matrix [40], [41]. For a matrix in $\mathbb{R}^{2\,\mathrm{x}\,2}$ an efficient approach based on the matrix characteristic equation also exists [42]. The principal square root can be obtained by selecting the result with eigenvalues in the open right half-plane.

To prove that the discrete steady-state covariance matrix is valid, we can first verify that it is symmetric. Take $\boldsymbol{B}$ to be the operand of the matrix square root.

$$\begin{aligned}
\boldsymbol{P}_{d,\infty} &= \boldsymbol{P}_d^T(\infty) \\
\boldsymbol{Q}_d\boldsymbol{B}^{\frac{1}{2}} &= \left[\boldsymbol{B}^{\frac{1}{2}}\right]^T\boldsymbol{Q}_d^T \\
\boldsymbol{B}^{\frac{1}{2}} &= \boldsymbol{Q}_d^{-1}\left[\boldsymbol{B}^{\frac{1}{2}}\right]^T\boldsymbol{Q}_d \\
\boldsymbol{B} &= \boldsymbol{Q}_d^{-1}\left[\boldsymbol{B}^{\frac{1}{2}}\right]^T\boldsymbol{Q}_d\boldsymbol{Q}_d^{-1}\left[\boldsymbol{B}^{\frac{1}{2}}\right]^T\boldsymbol{Q}_d \\
\boldsymbol{B} &= \boldsymbol{Q}_d^{-1}\boldsymbol{B}^T\boldsymbol{Q}_d \\
\boldsymbol{B} &= \boldsymbol{Q}_d^{-1}\left(\boldsymbol{R}_d\boldsymbol{Q}_d^{-1} + \frac{1}{4}\boldsymbol{I}\right)\boldsymbol{Q}_d \\
\boldsymbol{B} &= \boldsymbol{B}
\end{aligned}$$

The steady-state covariance equation is therefore symmetric. To verify that the result is positive definite, e.g. with positive eigenvalues, we can place the following upper bound on the expression.

$$\begin{aligned}
\boldsymbol{P}_{d,\infty} &= \boldsymbol{Q}_d\left[\left(\boldsymbol{Q}_d^{-1}\boldsymbol{R}_d + \frac{1}{4}\boldsymbol{I}\right)^{\frac{1}{2}} - \frac{1}{2}\boldsymbol{I}\right] \\
&> \boldsymbol{Q}_d\left(\boldsymbol{Q}_d^{-1}\boldsymbol{R}_d\right)^{\frac{1}{2}} \\
&= \boldsymbol{Q}_d^{\frac{1}{2}}\left(\boldsymbol{Q}_d^{-\frac{1}{2}}\boldsymbol{R}_d\boldsymbol{Q}_d^{-\frac{1}{2}}\right)^{\frac{1}{2}}\boldsymbol{Q}_d^{\frac{1}{2}}
\end{aligned}$$

The last equality is an identity for the matrix geometric mean (often denoted as $\boldsymbol{Q}_d\#\boldsymbol{R}_d$). Given positive definite input matrices, the geometric mean is also positive and unique; see [43]. We can therefore conclude that $\boldsymbol{P}_{d,\infty}$ is a valid covariance matrix for all positive definite $\boldsymbol{Q}_d$ and $\boldsymbol{R}_d$.

APPENDIX B
CONTINUOUS-TIME USBL ERROR COVARIANCE

We can also extend the result in the previous section to a continuous-time error covariance equation. If the rate of the updates are high relative to the simulation horizon or the cumulative effect of multiple USBL updates is more important than exactly representing individual updates, one can model the error covariance matrix as a continuous-time differential equation. The Kalman-Bucy filter is the continuous version of the Kalman filter [44]. The continuous Kalman filter can be derived from a discrete state space formulation [26, Appendix B.1].

$$\dot{\boldsymbol{P}} = \boldsymbol{F}\boldsymbol{P} + \boldsymbol{P}\boldsymbol{F}^T - \boldsymbol{P}\boldsymbol{H}^T\boldsymbol{R}^{-1}\boldsymbol{H}\boldsymbol{P} + \boldsymbol{G}\boldsymbol{Q}\boldsymbol{G}^T$$

Here the matrix $\boldsymbol{F}$ describes the continuous-time linear dynamics. In our case, all entries are equal to zero, as we have a system purely driven by its inputs plus noise. The measurement matrix, $\boldsymbol{H}$ is equal to the identity matrix since all states are directly measured. This leads to the simple differential equation below.

$$\dot{\boldsymbol{P}} = \boldsymbol{G}(t)\boldsymbol{Q}\boldsymbol{G}^T(t) - \boldsymbol{P}(t)\boldsymbol{R}_c^{-1}(t)\boldsymbol{P}(t)$$

In the original derivation, the measurement covariance was modified to account for the increase in sample rate, by setting $\boldsymbol{R}_c(t) \approx \boldsymbol{J}_U(t)\boldsymbol{\Sigma}_U\boldsymbol{J}_U^T(t)\Delta t_U$. This differential equation approximately tracks the mid-point between covariance updates. If we are interested in having the it track the bottom of the updates instead (e.g. the posterior values), we can compute a different measurement covariance by setting the differential equation equal to zero and inserting for the steady-state covariance.

$$\boldsymbol{R}_c(\infty) = \boldsymbol{P}_{d,\infty}\boldsymbol{Q}_c^{-1}\boldsymbol{P}_{d,\infty}$$

The continuous-time error covariance equation can be used to evaluate the variance reduction by following a given path but must be solved using numerical integration. Since the measurement equation is linearized, the equation is related to an *extended* Kalman-Bucy filter, without the linear dynamics. A comparison of the discrete and continuous error covariance equations is included in Fig. 3, where an AUV and ASV cross over each other in a straight line.

REFERENCES

[1] V. A. Huvenne, K. Robert, L. Marsh, C. L. Iacono, T. Le Bas, and R. B. Wynn, "ROVs and AUVs," in *Submarine Geomorphology*. Cham, Switzerland: Springer, 2018, pp. 93–108, doi: 10.1007/978-3-319-57852-1_7.

[2] O. Hegrenaes, A. Ramstad, T. Pedersen, and D. Velasco, "Validation of a new generation DVL for underwater vehicle navigation," in *Proc. IEEE/OES Auto. Underwater Vehicles (AUV)*, Tokyo, Japan, Nov. 2016, pp. 342–348, doi: 10.1109/AUV.2016.7778694.

[3] P. E. Hagen, O. Midtgaard, and O. Hasvold, "Making AUVs truly autonomous," in *Proc. MTS/IEEE OCEANS*, Vancouver, BC, Canada, Sep. 2007, pp. 1–4, doi: 10.1109/OCEANS.2007.4449405.

[4] L. Paull, S. Saeedi, M. Seto, and H. Li, "AUV navigation and localization: A review," *IEEE J. Ocean. Eng.*, vol. 39, no. 1, pp. 131–149, Jan. 2014, doi: 10.1109/JOE.2013.2278891.

[5] K. Zwolak, B. Simpson, B. Anderson, E. Bazhenova, R. Falconer, T. Kearns, H. Minami, J. Roperez, A. Rosedee, H. Sade, N. Tinmouth, R. Wigley, and Y. Zarayskaya, "An unmanned seafloor mapping system: The concept of an AUV integrated with the newly designed USV SEA-KIT," in *Proc. MTS/IEEE OCEANS*, Aberdeen, U.K., Jun. 2017, pp. 1–6, doi: 10.1109/OCEANSE.2017.8084899.

[6] M. V. Jakuba, C. L. Kaiser, C. R. German, A. S. Soule, and S. R. Kelley, "Toward an autonomous communications relay for deep-water scientific AUV operations," in *Proc. IEEE/OES Auto. Underwater Vehicle Workshop (AUV)*, Porto, Portugal, Nov. 2018, pp. 1–7, doi: 10.1109/AUV.2018.8729769.

[7] P. Norgren, M. Ludvigsen, T. Ingebretsen, and V. E. Hovstein, "Tracking and remote monitoring of an autonomous underwater vehicle using an unmanned surface vehicle in the Trondheim fjord," in *Proc. MTS/IEEE OCEANS*, Washington, DC, USA, Oct. 2015, pp. 1–6, doi: 10.23919/OCEANS.2015.7401975.

[8] M. Ludvigsen, S. M. Albrektsen, K. Cisek, T. A. Johansen, P. Norgren, R. Skjetne, A. Zolich, P. S. Dias, S. Ferreira, J. B. de Sousa, T. O. Fossum, O. Sture, T. R. Krogstad, O. Midtgaard, V. Hovstein, and E. Vagsholm, "Network of heterogeneous autonomous vehicles for marine research and management," in *Proc. OCEANS MTS/IEEE*, Monterey, CA, USA, Sep. 2016, pp. 1–7, doi: 10.1109/OCEANS.2016.7761494.

[9] J. Andersson, "A general-purpose software framework for dynamic optimization," Ph.D. dissertation, Arenberg Doctoral School, KU Leuven, Dept. Elect. Eng., (ESAT/SCD) Optim. Eng. Center, Kasteelpark Arenberg, Belgium, 2013.

[10] A. Wächter and L. T. Biegler, "On the implementation of an interior-point filter line-search algorithm for large-scale nonlinear programming," *Math. Program.*, vol. 106, no. 1, pp. 25–57, Mar. 2006, doi: 10.1007/s10107-004-0559-y.

[11] P. Bonami, P. Belotti, J. J. Forrest, L. Ladanyi, C. Laird, J. Lee, F. Margot, A. Waechter, L. T. Biegler, A. R. Conn, G. Cornuejols, A. Lodi, I. E. Grossmann, and N. Sawaya. (2020). *Basic Open-Source Nonlinear Mixed Integer Programming (BONMIN), Version 1.8.8*. [Online]. Available: https://www.coin-or.org/Bonmin

[12] P. Bonami, L. T. Biegler, A. R. Conn, G. Cornuéjols, I. E. Grossmann, C. D. Laird, J. Lee, A. Lodi, F. Margot, N. Sawaya, and A. Wächter, "An algorithmic framework for convex mixed integer nonlinear programs," *Discrete Optim.*, vol. 5, no. 2, pp. 186–204, May 2008, doi: 10.1016/j.disopt.2006.10.011.

[13] Computational Mathematics Group. (2015). *HSL. A Collection of Fortran Codes for Large Scale Scientific Computation, Version 2015.06.23*. [Online]. Available: http://www.hsl.rl.ac.uk/index.html

[14] M. F. Fallon, G. Papadopoulos, J. J. Leonard, and N. M. Patrikalakis, "Cooperative AUV navigation using a single maneuvering surface craft," *Int. J. Robot. Res.*, vol. 29, no. 12, pp. 1461–1474, Oct. 2010, doi: 10.1177/0278364910380760.

[15] A. Bahr, J. J. Leonard, and A. Martinoli, "Dynamic positioning of beacon vehicles for cooperative underwater navigation," in *Proc. IEEE/RSJ Int. Conf. Intell. Robots Syst.*, Vilamoura, Portugal, Oct. 2012, pp. 3760–3767, doi: 10.1109/IROS.2012.6386168.

[16] Y. T. Tan, R. Gao, and M. Chitre, "Cooperative path planning for range-only localization using a single moving beacon," *IEEE J. Ocean. Eng.*, vol. 39, no. 2, pp. 371–385, Apr. 2014, doi: 10.1109/JOE.2013.2296361.

[17] J. S. Willners, L. Toohey, and Y. Petillot, "Sampling-based path planning for cooperative autonomous maritime vehicles to reduce uncertainty in range-only localization," *IEEE Robot. Autom. Lett.*, vol. 4, no. 4, pp. 3987–3994, Oct. 2019, doi: 10.1109/LRA.2019.2926947.

[18] O. Hegrenaes, T. O. Sabo, P. E. Hagen, and B. Jalving, "Horizontal mapping accuracy in hydrographic AUV surveys," in *Proc. IEEE/OES Auto. Underwater Vehicles*, Monterey, CA, USA, Sep. 2010, pp. 1–13, doi: 10.1109/AUV.2010.5779662.

[19] V. H. Fernandes, D. D. Rodrigues, A. A. Neto, and L. G. Barbosa, "Modeling positional uncertainty for hydrographic surveys with AUV," *J. Surv. Eng.*, vol. 145, no. 1, Feb. 2019, Art. no. 04018014, doi: 10.1061/(ASCE)SU.1943-5428.0000269.

[20] T. I. Fossen, "Kinematics," in *Handbook of Marine Craft Hydrodynamics and Motion Control*. Chichester, U.K.: Wiley, 2011, ch. 2, sec. 2, pp. 20–34, doi: 10.1002/9781119994138.

[21] A. M. Lekkas and T. I. Fossen, "Line-of-sight guidance for path following of marine vehicles," in *Advanced in Marine Robotics*, G. Oren, Ed. Riga, Latvia: LAP Lambert Academic Publishing, Jun. 2013, pp. 63–92.

[22] B. Jalving, K. Gade, K. Svartveit, A. Willumsen, and R. Sørhagen, "DVL velocity aiding in the HUGIN 1000 integrated inertial navigation system," *Model., Identificat. Control, Norwegian Res. Bull.*, vol. 25, no. 4, pp. 223–236, 2004, doi: 10.4173/mic.2004.4.2.

[23] K. Gade, "The seven ways to find heading," *J. Navigat.*, vol. 69, no. 5, pp. 955–970, Sep. 2016, doi: 10.1017/S0373463316000096.

[24] B. Jalving, E. Bovio, and K. Gade, "Integrated inertial navigation systems for AUVs for REA applications," in *Proc. MREP*. La Spezia, Italy: NATO SACLANT Undersea Research Centre, May 2003, pp. 1–23.

[25] O. J. Woodman, "An introduction to inertial navigation," Comput. Lab., Univ. Cambridge, Cambridge, U.K., Tech. Rep. UCAM-CL-TR-696, Aug. 2007.

[26] R. G. Brown and P. Y. Hwang, "Mathematical description of random signals," in *Introduction to Random Signals and Applied Kalman Filtering: With MATLAB Exercises* 4th ed., Hoboken, NJ, USA: Wiley, 2012, ch. 2, sec. 9, pp. 77–81.

[27] P. Bromiley, "Products and convolutions of Gaussian probability density functions," Div. Inform., Imag. Data Sci., School Health Sci., Univ. Manchester, Stopford Building, Manchester, U.K., Tech. Rep. Memo 2003–003, 2018. [Online]. Available: http://www.tina-vision.net/docs/memos/2003-003.pdf

[28] W. W. Hager, "Updating the inverse of a matrix," *SIAM Rev.*, vol. 31, no. 2, pp. 221–239, Jun. 1989, doi: 10.1137/1031049.

[29] L. Grüne and J. Pannek, "Numerical optimal control of nonlinear systems," in *Nonlinear Model Predictive Control*. London, U.K.: Springer, 2011, ch. 10, sec. 1, pp. 275–288.

[30] H. G. Bock and K.-J. Plitt, "A multiple shooting algorithm for direct solution of optimal control problems," *IFAC Proc. Volumes*, vol. 17, no. 2, pp. 1603–1608, Jul. 1984, doi: 10.1016/S1474-6670(17)61205-9.

[31] R. Cagienard, P. Grieder, E. C. Kerrigan, and M. Morari, "Move blocking strategies in receding horizon control," *J. Process Control*, vol. 17, no. 6, pp. 563–570, Jul. 2007, doi: 10.1016/j.jprocont.2007.01.001.

[32] D. G. Watson, "Powering I," in *Practical Ship Design*, vol. 1, Oxford, U.K.: Elsevier, 1998, ch. 6, sec. 3, pp. 162–171.

[33] G. Bitar, M. Breivik, and A. M. Lekkas, "Energy-optimized path planning for autonomous ferries," *IFAC-PapersOnLine*, vol. 51, no. 29, pp. 389–394, Sep. 2018, doi: 10.1016/j.ifacol.2018.09.456.

[34] D. Q. Mayne, J. B. Rawlings, C. V. Rao, and P. O. M. Scokaert, "Constrained model predictive control: Stability and optimality," *Automatica*, vol. 36, no. 6, pp. 789–814, 2000, doi: 10.1016/S0005-1098(99)00214-9.

[35] M. B. Porter, "The bellhop manual and user's guide: Preliminary draft," Heat, Light, Sound Res., Inc., La Jolla, CA, USA, Tech. Rep. HLS-2010-1, 2010. [Online]. Available: https://oalib-acoustics.org/Rays/HLS-2010-1.pdf

[36] M. V. Jakuba, J. C. Kinsey, J. W. Partan, and S. E. Webster, "Feasibility of low-power one-way travel-time inverted ultra-short baseline navigation," in *Proc. MTS/IEEE OCEANS*, Washington, DC, USA, Oct. 2015, pp. 1–10, doi: 10.23919/OCEANS.2015.7401992.

[37] N. R. Rypkema, E. M. Fischell, and H. Schmidt, "One-way travel-time inverted ultra-short baseline localization for low-cost autonomous underwater vehicles," in *Proc. IEEE Int. Conf. Robot. Autom. (ICRA)*, Singapore, May 2017, pp. 4920–4926, doi: 10.1109/ICRA.2017.7989570.

[38] C. R. Johnson, "Positive definite matrices," *Amer. Math. Monthly*, vol. 77, no. 3, pp. 259–264, Mar. 1970, doi: 10.2307/2317709.

[39] N. J. Higham, "Background: Definitions and useful facts," in *Functions of Matrices: Theory and Computation*. Philadelphia, PA, USA: SIAM, 2008, sec. 4, pp. 323–324, doi: 10.1137/1.9780898717778.

[40] N. J. Higham, "Computing real square roots of a real matrix," *Linear Algebra Appl.*, vols. 88–89, pp. 405–430, Apr. 1987, doi: 10.1016/0024-3795(87)90118-2.

[41] E. Deadman, N. J. Higham, and R. Ralha, "Blocked Schur algorithms for computing the matrix square root," in *Proc. Int. Workshop Appl. Parallel Comput.*, Helsinki, Finland, Jun. 2012, pp. 171–182, doi: 10.1007/978-3-642-36803-5_12.

[42] B. W. Levinger, "The square root of a 2×2 matrix," *Math. Mag.*, vol. 53, no. 4, pp. 222–224, 1980, doi: 10.2307/2689616.

[43] R. Bhatia, "Matrix means," in *Positive Definite Matrices*. Princeton, NJ, USA: Princeton Univ. Press, 2007, ch. 4, sec. 1, pp. 103–111, doi: 10.1515/9781400827787.101.

[44] R. E. Kalman and R. S. Bucy, "New results in linear filtering and prediction theory," *J. Basic Eng.*, vol. 83, no. 1, pp. 95–108, Mar. 1961, doi: 10.1115/1.3658902.

ØYSTEIN STURE received the M.Sc. degree in engineering cybernetics from the Norwegian University of Science and Technology (NTNU), in 2015, where he is currently pursuing the Ph.D. degree in seabed mapping with autonomous underwater vehicles using acoustic and optical instruments. His thesis work was performed in collaboration with SINTEF, where he continued to work on topics related to computer vision and machine learning in the aquaculture industry. His research interests include autonomy, computer science, applied statistics, underwater robotics, acoustics, and optics. His Ph.D. work was funded by MarMine, a project focused on research related to exploitation and exploration methodologies related to seafloor massive sulfide deposits on the Arctic Mid-Ocean Ridge.

PETTER NORGREN (Graduate Student Member, IEEE) received the M.Sc. degree in engineering cybernetics and the Ph.D. degree in marine cybernetics from the Norwegian University of Science and Technology (NTNU), in 2011 and 2018, respectively. From 2012 to 2013, he was with Marine Cybernetics AS involved in hardware-in-the-loop testing of marine control systems. He begun the Ph.D. Scholarship with the Department of Marine Technology, NTNU, in 2013, involved in autonomous underwater vehicles for arctic marine operations. He is currently a Postdoctoral Fellow with NTNU, involved in the Nansen Legacy programme. His research interests include AUVs for arctic marine operations and research, simultaneous localization and mapping, autonomous exploration, and tracking and monitoring of AUVs using USVs.

MARTIN LUDVIGSEN received the M.Sc. and Ph.D. degrees in marine technology from the Norwegian University of Science and Technology (NTNU), Trondheim, Norway, in 2001 and 2010, respectively. In 2009, he participated in the startup of the Applied Underwater Robotics Laboratory (AURLab), NTNU, where he remains in the position as manager. Since 2014, he has also been a Professor of underwater technology with the Department of Marine Technology, NTNU. In 2015, he was announced Adjunct Professor of marine technology with The University Centre in Svalbard, Longyearbyen, Svalbard, Norway. In 2015, he was a co-Founder of the NTNU technology spin-off Blueye robotics. The research portfolio includes applications of underwater vehicles and technology for marine mining, arctic operations, and marine science and developments within autonomy together with optical and acoustical seabed documentation.